https://ntrs.nasa.gov/search.jsp?R=19710028386 2020-03-11T21:35:00+00:00Z

N71 37862

NASA CR-
WRL 31650-31-T

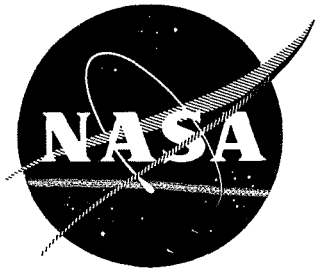

WATER-DEPTH MEASUREMENT BY WAVE REFRACTION AND MULTISPECTRAL TECHNIQUES

by

W. L. Brown, F. C. Polcyn, A. N. Sellman, and S. R. Stewart

INFRARED AND OPTICS LABORATORY
WILLOW RUN LABORATORIES
INSTITUTE OF SCIENCE AND TECHNOLOGY
THE UNIVERSITY OF MICHIGAN

prepared for

NATIONAL AERONAUTICS AND SPACE ADMINISTRATION

NASA Manned Spacecraft Center
NAS 9-9784
L. B. York/TF, Project Manager

CASE FILE
COPY

NOTICES

Sponsorship. The work reported herein was conducted by the Willow Run Laboratories of the Institute of Science and Technology for the National Aeronautics and Space Administration under NASA Contract NAS 9-9784, with L. B. York/TF, Earth Observations Division as Project Manager. Contracts and grants to The University of Michigan for the support of sponsored research are administered through the office of the Vice-President for Research.

Disclaimers. This report was prepared as an account of Government-sponsored work. Neither the United States, nor the National Aeronautics and Space Administration (NASA), nor any person acting on behalf of NASA:

(A) Makes any warranty or representation, expressed or implied with respect to the accuracy, completeness, or usefulness of the information contained in this report, or that the use of any information, apparatus, method, or process disclosed in this report may not infringe privately owned rights; or

(B) Assumes any liabilities with respect to the use of, or for damages resulting from the use of any information, apparatus, method, or process disclosed in this report.

As used above, "person acting on behalf of NASA" includes any employee or contractor of NASA, or employee of such contractor, to the extent that such employee or contractor of NASA or employee of such contractor prepares, disseminates, or provides access to any information pursuant to his employment or contract with NASA, or his employment with such contractor.

Availability Notice. Requests for copies of this report should be referred to:

National Aeronautics and Space Administration
Scientific and Technical Information Facility
P. O. Box 33
College Park, Md. 20740

Final Disposition. After this document has served its purpose, it may be destroyed. Please do not return it to the Willow Run Laboratories.

NASA CR-
WRL 31650-31-T

TECHNICAL REPORT

WATER-DEPTH MEASUREMENT BY WAVE REFRACTION AND MULTISPECTRAL TECHNIQUES

by

W. L. Brown, F. C. Polcyn, A. N. Sellman, and S. R. Stewart

INFRARED AND OPTICS LABORATORY
WILLOW RUN LABORATORIES
INSTITUTE OF SCIENCE AND TECHNOLOGY
THE UNIVERSITY OF MICHIGAN

prepared for

NATIONAL AERONAUTICS AND SPACE ADMINISTRATION

August 1971

NAS 9-9784

NASA Manned Spacecraft Center
Houston, Texas
L. B. York/TF, Project Manager
Earth Observations Division

FOREWORD

This report describes part of a comprehensive and continuing program of research into remote sensing of the environment from aircraft and satellites. The research is being carried out by the Willow Run Laboratories, a unit of The University of Michigan's Institute of Science and Technology, for the NASA Manned Spacecraft Center, Houston, Texas. The basic objective of this multidisciplinary program is to develop remote sensing as a practical tool, to quickly and economically provide the planner and decision-maker with extensive information.

Timely information from remote sensing will be important to the farmer, the city planner, the conservationist, and others concerned with problems such as crop yield and disease, urban land studies and development, water pollution, and forest management. The scope of our program includes: extending understanding of basic processes; developing new applications for remote sensing; evolving advanced remote sensing systems and automatic data processing to extract information in a useful form; and assisting in data collection, processing, and analysis, to include material spectra and ground-truth verification.

The research described herein was performed under NASA Contract NAS 9-9784, and covers the period from 1 July 1969 through 30 September 1970. The program was directed by R. R. Legault, Associate Director of Willow Run Laboratories. Principal Investigator was Jon D. Erickson. The work was done under the management of the NASA Contract Monitor, L. B. York/TF, Manned Spacecraft Center. The Willow Run Laboratories' number for this report is 31650-31-T.

ABSTRACT

Two remote sensing techniques which measure water depth have been investigated. One technique involves photographic observation of wave-refraction phenomena and of wave-length changes measured in Fourier transforms. The transforms were obtained by optical processing. Test sites near Puerto Rico and Barbados were used to study wave changes which occur near nonuniform bottom profiles of shallow reefs.

The second technique makes use of a multispectral scanner to measure radiation reflected from the ocean floor. Measurement occurs in several spectral intervals in the visible region. The depth is calculated when we take the ratio of signals in pairs of spectral bands. The technique was tested for sloping sandy beach gradients, as well as for coral reef areas which contained a variety of materials of different reflectances. Examples of computer-generated depth maps are included.

CONTENTS

FIGURES

TABLES

WATER-DEPTH MEASUREMENT BY WAVE REFRACTION AND MULTISPECTRAL TECHNIQUES

SUMMARY

The purpose of the research reported herein is to investigate the usefulness of detection and measurement of shallow water features, through the observation of the effects of these shoals or reefs on local sea state and/or upon the selective spectral reflectance of the incident radiation. This research uses aerial photography and multispectral scanner imagery to record the wave surface and radiance at various locations. Procedures for the production and use of optical transforms of the sea surface are explained. It is shown that optical Fourier analysis of photography can produce valuable information about both sea-state characteristics and wave-refraction phenomena. Also, the advantages of processing imagery, dominated by a single, well defined wave set, are demonstrated.

We employed a second technique for measuring depth, in which we used the multispectral scanner output which was recorded on analog tapes during the data-collection missions. An explanation of how the data were digitized and analyzed is included.

Both techniques proved to be feasible within certain operational constraints. The wave-refraction method depends on the existence of a set of wave swells, the wave length of which is long enough to be affected by the presence of a shallow feature. The multispectral ratio technique is being developed as a complementary method to provide a depth measurement at all image points at which a bottom reflection can be measured.

1 INTRODUCTION

This report is the third in a series which describes the research effort being made by The University of Michigan to use remote sensing techniques to locate and measure shallow water depths. The first two reports (Refs. 1 and 2) gave the results of the initial survey of techniques which identified the more useful observables and which demonstrated initial feasibility of two of the methods currently being developed. The earlier work was done under contract with the Spacecraft Oceanography Project, NAVOCEANO, under management of John Sherman III, who also coordinated this year's effort, performed under NASA Contract NAS 9-9784.

The purpose of the investigation reported herein was to determine how changes in local sea state and differences in spectral reflectances could be used to detect and measure shallow-water

features. More specifically, we were interested in relating the measurable changes in observable quantities, such as wave length* and spectral intensity. In this research, we used aerial photography and multispectral scanner imagery to record the wave surface and radiance at various locations. The photographic transparencies were then analyzed via an optical processor to produce measurable Fourier transform frequencies which are related to the wave surface. Comparisons of deep- to shallow-water wave lengths at probable sites were then made in order to compute shallow-depths. Section 2 explains depth measurement from wave-refraction analysis, and it includes a discussion of the equipment setup and preliminary experiments, as well as the depth determinations reached at selected test sites.

In the second technique for measuring depth, we use the signals collected by a multispectral scanner. These signals were recorded on analog tapes during the data-collection missions, subsequently digitized, and, finally, analyzed via a CDC-1604 digital computer. The signals, carried in 12 separate tape channels, represent the relative intensity of the scene on a point-by-point basis, and enabled us to determine (with the use of a calibrated sun sensor) the spectral reflectances on a high-resolution basis. Details of the analytical procedure are explained in subsequent portions of this report. Section 3 discusses the application of remotely sensed multispectral data to the determination of water depth. Conclusions are presented in Section 4. Appendix I reviews the imagery collected during Mission No. 98 and outlines its possible value in achieving mission objectives. Appendix II discusses the empirical determination of attenuation coefficients and bottom reflectances.

2
DEPTH MEASUREMENT FROM WAVE-REFRACTION ANALYSIS

The detection of shallow water by changes in wave state has been attempted by a variety of techniques. Interpretation of aerial photography allowed researchers to detect and measure the influence of shallow water on wave action [3, 4]. It is well known that this influence is primarily on the wave length and wave direction. More specifically, as a set of waves approaches shallow water, the wave length will decrease as it feels bottom. If the wave train is approaching the shallow area at an angle, the longitudinal orientation of the wave train will refract, causing the wave train to approach the shoreline in a mode parallel, or nearly parallel, to the shoreline.

Recent studies have made use of another approach for detecting the presence of shallow water. Polcyn and Sattinger [2] analyzed wave motion via optically generated Fourier transforms. This procedure uses photographic imagery, collected from aircraft or spacecraft, of reflected sunglitter patterns on water surfaces. The technique makes use of the observable changes in wave

* Throughout this report, care must be taken to distinguish the two-word term "wave length," referring to the water surface, from the one-word term "wavelength," referring to the radiation spectrum.

motion, as a set of waves moves from a deep- to shallow-water location. Both wave-length changes and wave-refraction angles are detectable when a coherent light source (laser) is used in an optical processor to generate a Fourier transform to give frequency and directional characteristics.* The deep-water transform is compared to the shallow-water transform to derive changes in wave state. The results of the comparison lead to measurements of the change in depth.

The sea-state condition at the time of imagery collection is extremely important for optical processing techniques. "The simplest model consists of a set of sinusoidal waves, having one frequency and one direction" [6]. The wave train in Jobos Bay, along the southern coast of Puerto Rico, closely duplicates this model. This area and its transform are shown in Fig. 1. The data were collected by NASA (Houston) as part of Mission No. 98 under the NASA Earth Resources Program. (See Appendix I.)

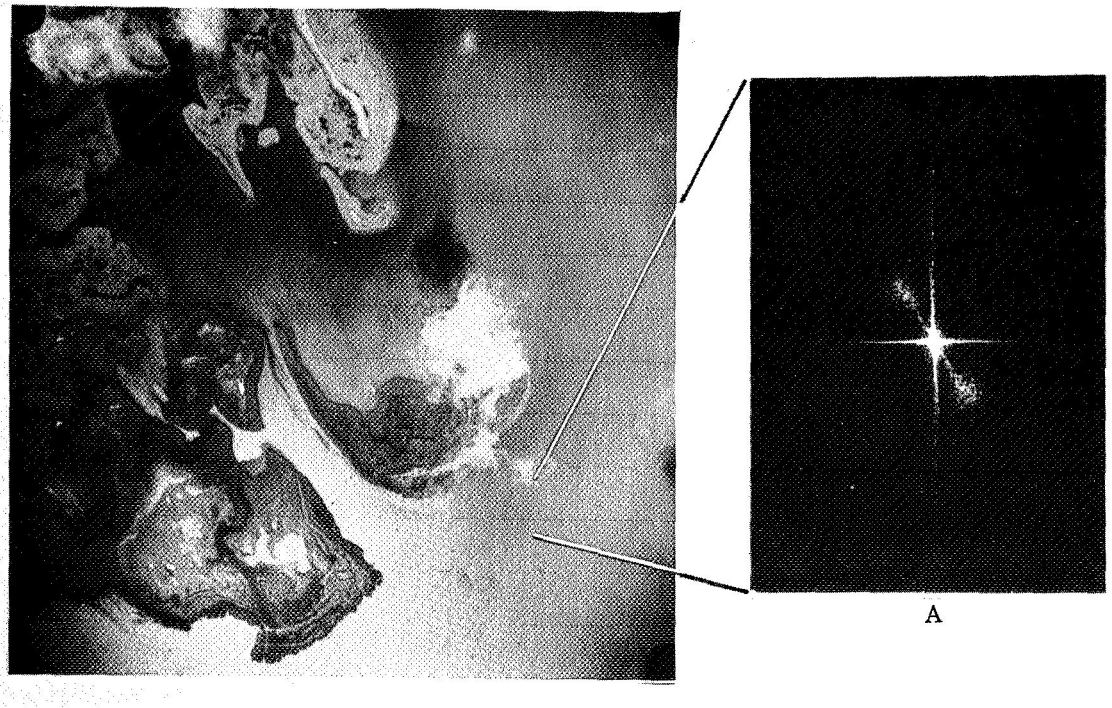

FIGURE 1. SEA STATE OF A MODERATELY WELL DEFINED SWELL AND ITS FOURIER TRANSFORM, PUERTO RICO

*This is not a new process. In 1949, Barber [5] used an arc lamp as a light source and successfully produced diffraction patterns of wave state which showed both low and high frequency components.

The diffraction pattern discloses several important features about the sea state. In the transform process, the lowest frequencies occur closest to the center of the pattern and increase with the radial distance from the center. Thus, the low-frequency wave set (swell) appears near the center of the diffraction pattern as opposing dots. The cluster farther out discloses a higher frequency wave set in the bay. The linearity of the total pattern indicates that all the wave sets are moving either in the same direction (SW to NE) or in directions exactly opposite to each other. Close inspection of the imagery substantiates the former interpretation.

Most of the wave imagery collected for this mission does not have this simple, well defined character. It is much more complex than the ideal, revealing wave sets which have differing propagation directions, wave lengths, and wave heights. The result is a reflected sun-glitter image which, in many cases, is devoid of obvious pattern. Furthermore, the sun-glitter pattern may not display the important, longer wave lengths to best advantage.

The importance of collecting imagery which displays waves of very great length is substantiated by the relationship of detectable depth versus wave length. This relationship is illustrated in Fig. 2, which we have reproduced from the first report in this series [1]. From the wavelength ratio of shallow water to deep water (L/L_d), a corresponding relative depth can be extracted from the abscissa (d/L_d). Shoal depths are then calculated by multiplying the relative depth by the deep water wave length. Potentially, the longer the wave length, the deeper one can detect. Thus, the use of changes in detectable wave length to measure shoal water depths is most successful when we use imagery of waves which are simplest in form and are relatively long at the depth locations to be measured.

2.1. EQUIPMENT SETUP FOR OPTICAL FOURIER ANALYSIS

The diagram in Fig. 3 illustrates the equipment setup used in our research. The dotted line represents the laser-beam path. Two camera formats were tested, a speed Graphic with a Polaroid film back and a lensless 35-mm single-lens reflex. The latter was selected because it gives greater latitude in selecting film types which have desirable speed and resolution characteristics.

Transforms were photographed from black and white transparencies made on mylar-base Kodalith sheets of the aerial photographs and from the color aerial photography directly. For the objectives of this research, it was not necessary for the image plane to be optically flat.

In order to equate the measurements taken from the photographed transform with the actual scale of the aerial photography, a ronchi grating of known frequency (100 lines/in.) was photographed in each test.

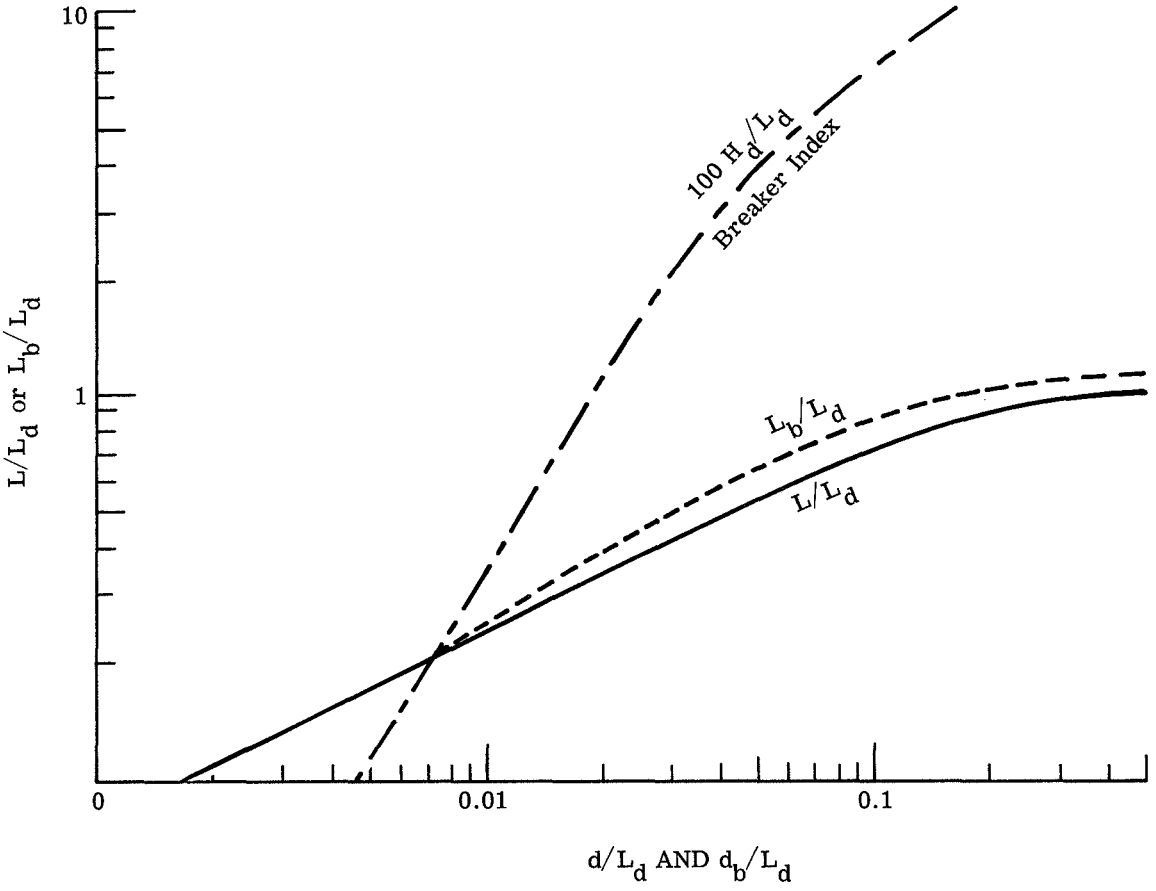

FIGURE 2. CHANGE DURING SHOALING IN WAVE-LENGTH RATIO VERSUS RELATIVE DEPTH

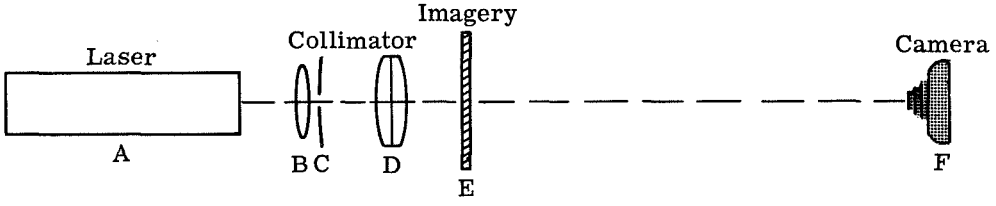

FIGURE 3. OPTICAL-BENCH SETUP FOR FOURIER PROCESSOR

2.2. PRELIMINARY EXPERIMENTS WITH FOURIER OPTICAL TRANSFORMS

Two tests of optical transform characteristics were performed in order to facilitate the interpretation of transform photographs.

We observed that individual wave sets were not uniformly represented throughout the reflected sun-glitter pattern. Instead, they were more distinct at the point at which their propagation line was tangent to the pattern and less distinct at other points. Second, some bending of the wave sets also appeared to take place on either side of the tangency point. Thus, an individual wave set would be most distinct at two opposite points in the reflected sun-glitter pattern.

The geometry of surface reflections may pose a problem for correlating accurate measurements of wave length. We were confident that transforms of wave state at or near the principal point of the photograph would represent reflected sunlight from the same point on each wave. It was possible that, as the look angle was increased outward toward the edge of the scene, the reflected sunlight would not be coming from the same point on each wave. This could easily result in the same wave set having two different lengths, depending upon where it was measured with respect to the principal point.*

Figure 4 shows a frame of deep-water imagery (from an altitude of 10,000 ft) between St. Croix and St. John, as well as four transforms photographed at opposing points on the reflected sun-glitter pattern. Two wave sets, which move from the top to the bottom of the photograph, are clearly transformed in photograph C. A third wave set, which moves diagonally from A to D, is apparent in transform photographs A, B, and D.

There are two significant points observable from these transforms. First, it would appear as though the frequency of the wave set has increased as it has moved from A, near the principal point, toward the lower portion of the photograph. Also, from A to B, the orientation of the wave set seems to have shifted slightly. We know that these changes on the wave imagery did not occur because of shoal influence or actual impingement. They are representative of the situation just described; that is, depending upon where the waves are measured in the imagery, artificial changes can be observed.

The situation is not as troublesome as it might appear. Since all portions of a scene in vertical photography are recorded at a uniform scale, and since we are interested in relative changes between deep- and shallow-water wave characteristics, this experiment suggests that we must consider measurements between wave sets that are as equidistant from the principal point as possible. In no case did we attempt to compare a wave set measured at or near the principal point with one near the edge of the scene.

*In true vertical photography of a horizontal object plane, which we are assuming is our situation, the image plane records objects at a uniform scale. This is not the case of oblique aerial photography, and pertinent adjustments must be made in this case [7].

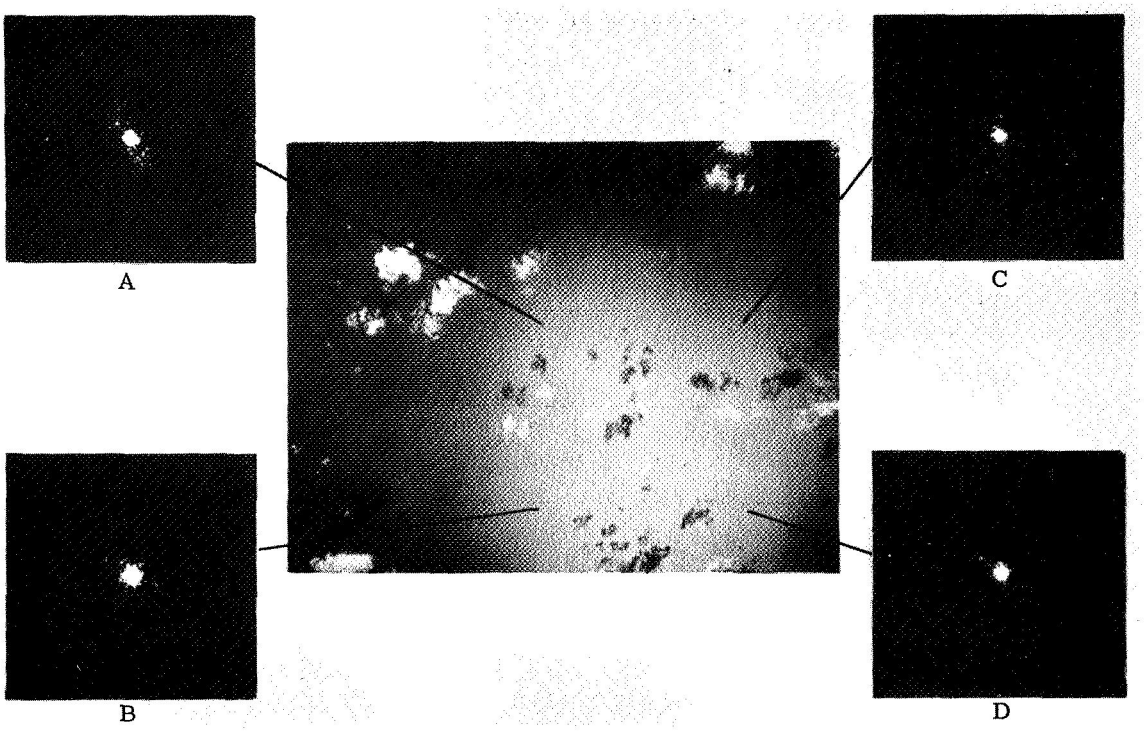

FIGURE 4. EFFECT OF SUN GLITTER PATTERN ON FOURIER TRANSFORM

A second test was conducted to determine the effect of aperture shape on the wave-transform pattern, an effect considered by Lendaris and Stanley [8]. Figure 5 shows the three apertures tested and the consequent transform results. All three transforms are of the same scene, photographed at the same speed, and printed on the same paper. Both the square and circular apertures produce added transform information and both tend to obscure the wave-frequency components of interest. This could be especially important for the square aperture, if the orientation of the wave train were coincident with either the horizontal or vertical axis of the aperture.

The apodizing filter has a clear center, with a concentric pattern which increases in density away from center. It is essentially a circular aperture; but it has no distinct edge which will transform to obscure the wave-train imagery under investigation. Transforms for which this filter was used produced the most distinct and unambiguous results. Results from test work done early in the report period were produced with the use of a square aperture, but the apodizing technique was adopted for a majority of the wave-analysis work.

2.3. DEPTH DETERMINATIONS BY USE OF FOURIER TRANSFORM METHOD ON HIGH ALTITUDE OF SELECTED TEST SITES

This section reports on five different test sites at which attempts were made to detect shoal depths. No depths were computed for the first two sites. This failure suggests constraints on

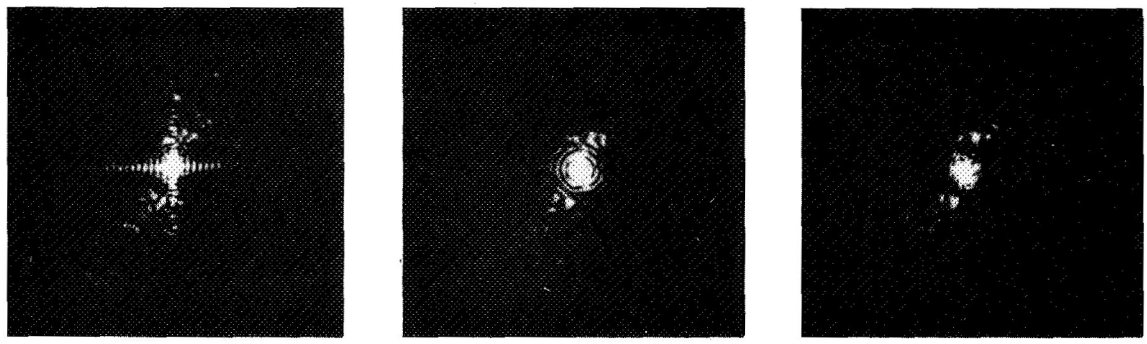

Square Circular Apodized

FIGURE 5. FOURIER TRANSFORMS, TAKEN WITH VARYING APERTURES

our choice of technique and is informative in that respect. The last three tests were successful because depths which conformed with the U. S. Coast and Geodetic Survey navigation charts were computed.

2.3.1. PUERTO RICO, PUNTA FIGURAS AREA

Figure 6 shows a reduced print of the first test site, the shoal Arrecife Algarrabo, near Punta Figuras, on the south shore of Puerto Rico. Figure 7 shows 3× enlargements of the optical transforms, photographed at indicated areas A, B, and C. The diffraction pattern from area A was used as the deep-water position for comparative measurements of wave-length changes noted in area B (which leads directly onto the shoal) and area C (approximately 800 ft away from the shoal). The depth of the water at A is only 30 ft, but as will be shown, moderate depth is of little consequence.

The low-frequency wave set, which runs approximately south to north in area A, transformed into the symmetrical dot pattern along the vertical axis of the diffraction pattern. This pattern was measured and gave a wave length of about 66 ft. Careful inspection of the pattern reveals that the remaining wave sets are clustering about the vertical axis, predominantly between 90° and 100° from the horizontal axis.

The diffraction patterns for areas B and C disclose numerous wave sets which provide wave-length comparison. Again, the majority of waves cluster about the vertical axis, between 90° and 130°. The high density of the transform near the center of diffraction patterns B and C makes it difficult to extract unambiguous points for measurement, so a comparison can be made with the deep-water transform of area A.

Theoretical calculations for shoal detection suggest where one ought to look for information (i.e., how close to the center of the pattern will a given wave length component be imaged). First, the 66-ft wave length for the deep-water wave swell indicates that shoal detection of approximately

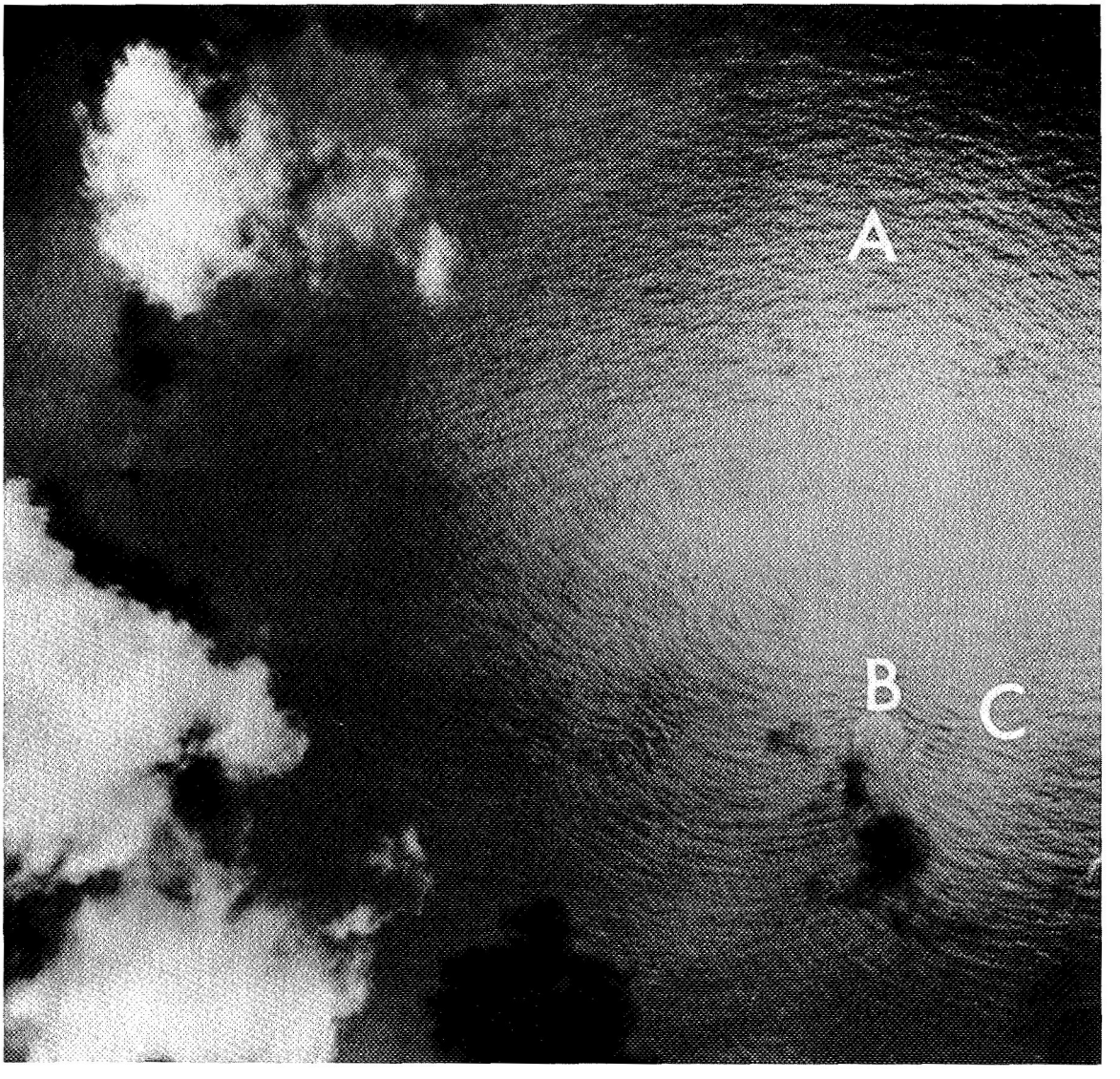

FIGURE 6. PHOTO OF SHOAL, ARRECIFE ALGARROBO, PUERTO RICO

30 ft (1/2 of the length) or less is possible. The hydrographic charts show water about 12-ft deep immediately around the shoal, so one can arbitrarily assume a 15-ft depth-detection goal. A 66-ft wave in 30 ft of water (area A) would decrease in length to 60 ft at a 15-ft depth. It was found that a 60-ft length would produce a transform with a frequency spread as shown in the diffraction patterns of B and C (Fig. 7). The frequency spread falls in the fully exposed region of that transform. While the transform may have the necessary information to detect a depth of 15 ft, the useful frequency information may well be partially or totally hidden in the center of the

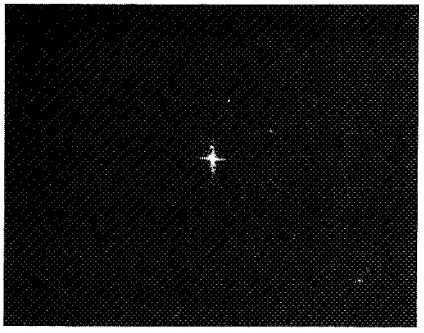

(a) Area A

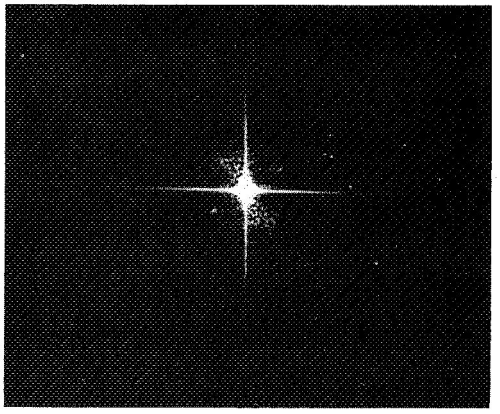

(b) Area B

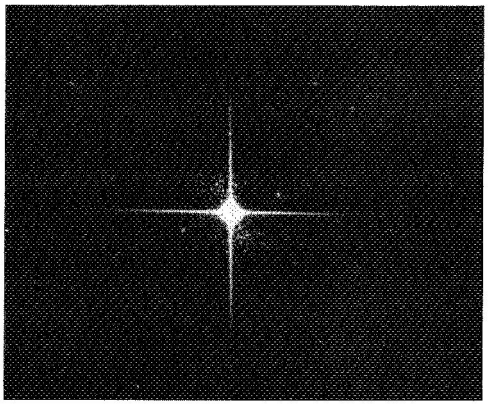

(c) Area C

FIGURE 7. DIFFRACTION PATTERNS PRODUCED FROM TEST SITE IN PUERTO RICO

diffraction pattern. This particular problem prompted us to change our equipment in favor of an apodizing filter, the benefits of which have already been discussed (Section 2.2).

2.3.2. BARBADOS

The second area chosen for optical processing was the long, narrow shoal (coral reef) which runs parallel to the southeastern shore of Barbados. Figure 8 shows both a reduced photograph of this area taken from the color Ektachrome imagery and a nautical chart with depth soundings (fathoms). The shoal lies about 1 mile offshore and has an average depth of approximately 50 ft (8 to 9 fathoms). On the shore side of the shoal, the depth averages 130 ft (22 fathoms), but is much greater seaward. Note that the shoal ends abruptly about 1 1/2 miles due south of South Point.

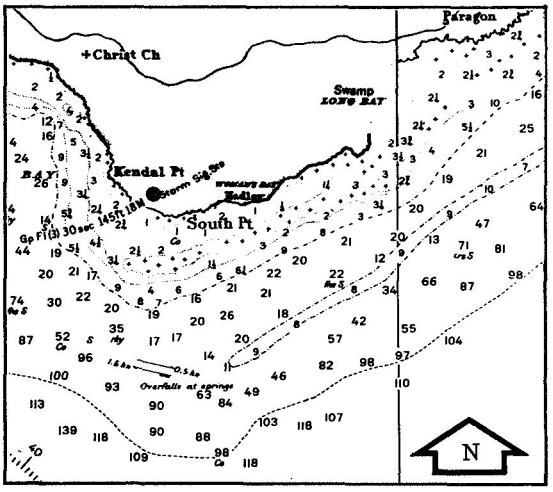

Approximate Scale 1:71,000

FIGURE 8. PHOTO OF SHOAL OFF BARBADOS AND NAUTICAL CHART WITH DEPTH SOUNDINGS

This shoal area was selected for analysis for two reasons. First, the flight was flown at 15,000 ft, which caused a noticeable reduction in scale as compared to the first test site. Second, a major set of waves was moving in a direction parallel to the shoal. Changes in wave length and/or wave refraction have had time to develop over the total length of the shoal. The shoal begins west of Kitridge Point and runs southwest for over 11 miles, until it ends at South Point.

Figure 9 depicts a simplified drawing of the area and includes three diffraction patterns produced on or near the shoal. It might have been preferable to work nearer the end of the shoal; however, the wake from one small boat (50-ft long), seen near the end of the shoal, would obviously interfere with the normal wave motion. Therefore, all optical processing was conducted east of this artificial disturbance.

The diffraction patterns clearly show the propagation direction of the two major wave sets. The set moving southwest, parallel to the shore, can easily be identified in the first and third quadrants. The other major set is moving onshore from the southeast. This wave set is not at all apparent in the photograph near the shoal, but was noted in the photographs from the first test site.

The diffraction patterns still do not disclose information that clearly relates to specific changes in wave motion, whether in length change or wave refraction. The dot pairs seen in all three patterns (first and third quadrants) represent wave lengths of 34 ft (A), 39 ft (B) and 42 ft (C): each is too short to detect a shoal depth of 50 ft. Again, the low-frequency wave information needed

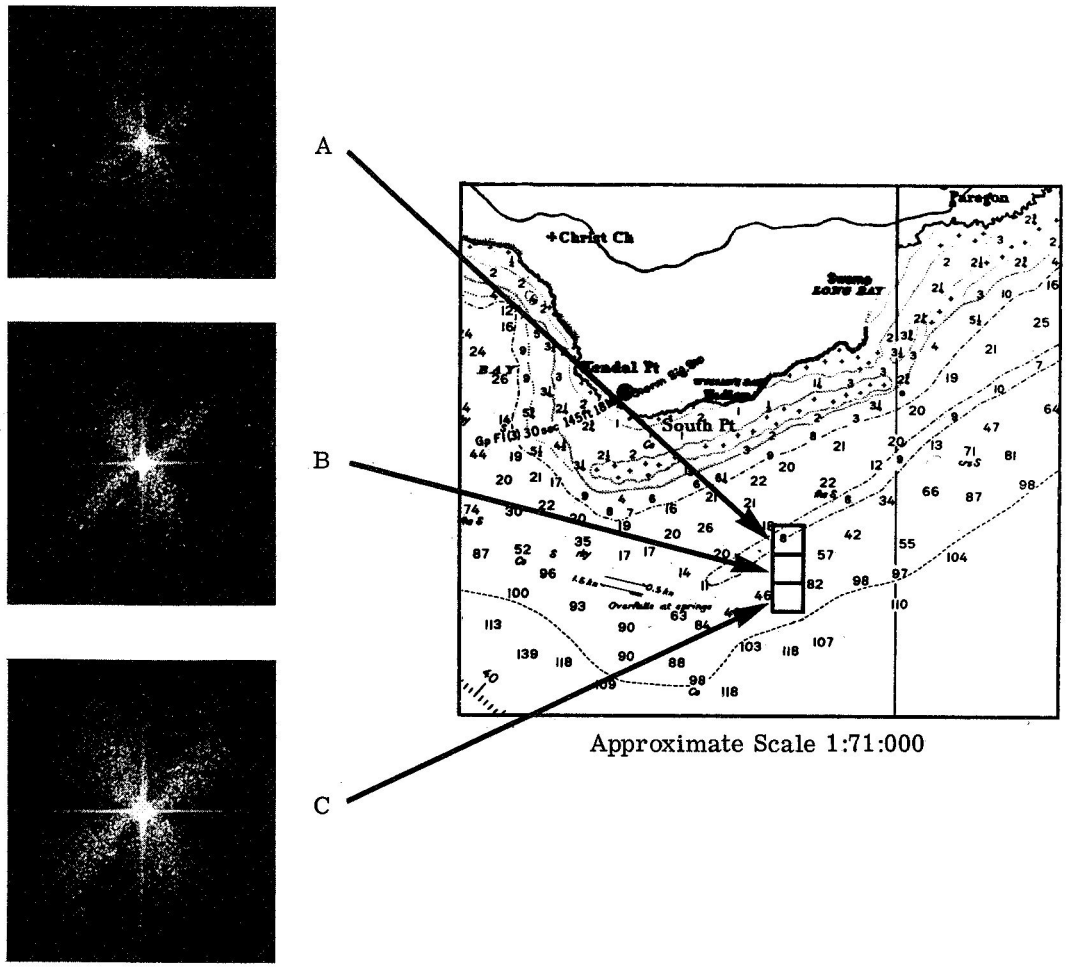

FIGURE 9. THREE DIFFRACTION PATTERNS PRODUCED NEAR SHOAL (BARBADOS)

to detect depths of 50 ft would transform very near the center of the star pattern. The diffraction patterns have a great deal of low-frequency information—too much, in fact, to give one unambiguous points for wave-length measurement.

The dot pairs do show a measureable change in direction, however. A and B are moving at an angle of 240°, while C is moving at an angle of 235°. The difficulty of equating this change specifically with the presence of the shoal remains.

2.3.3. PUERTO RICO, PUNTA BREA AREA

Figure 10 shows a reduced print of the third test site, a submerged shoal off Punta Brea, Puerto Rico. The lower transform depicts a deep-water wave swell that is 160 ft long. The shallow-water transform was measured on the same wave set as it passed just east of the sub-

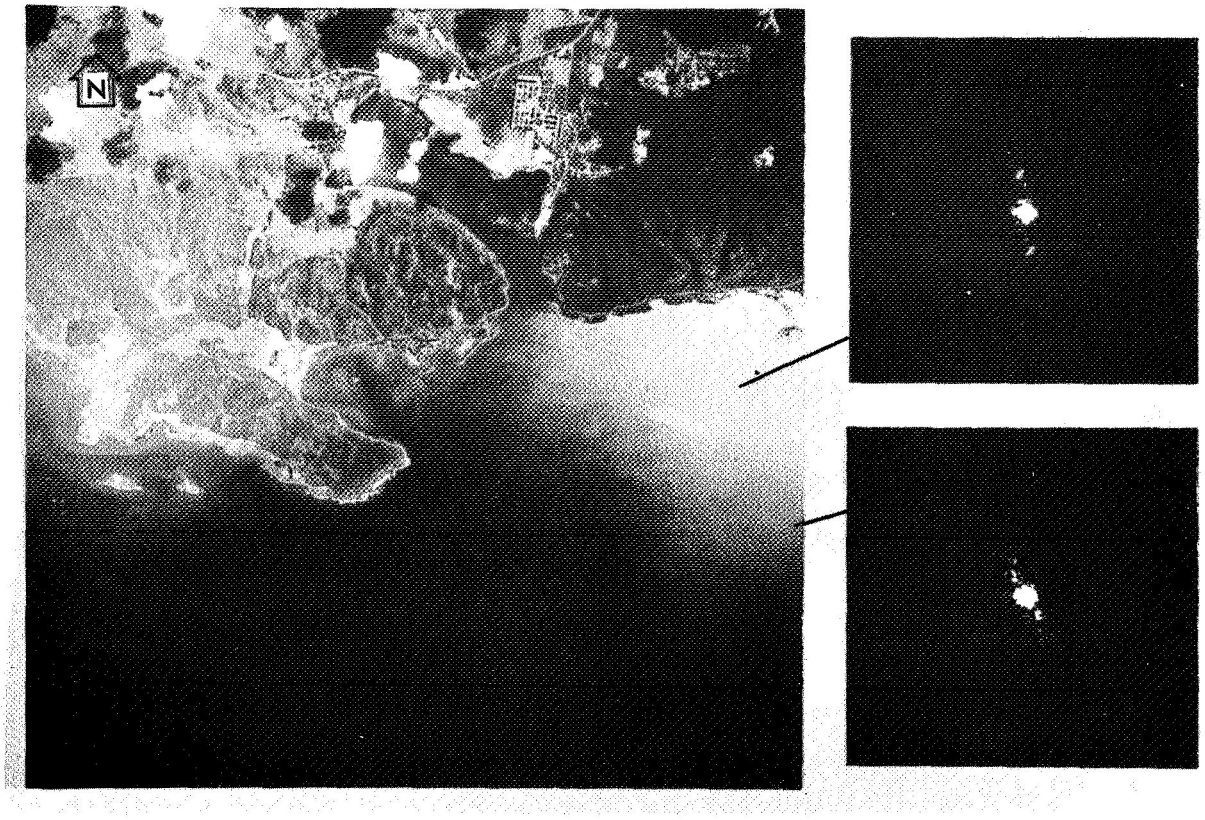

FIGURE 10. WATER-DEPTH MEASUREMENT OFF PUNTA BREA, PUERTO RICO

merged shoal and into shallower water. Here, it measured 87 ft. The partial refraction of the wave set to more a northerly propagation direction was caused by a shoal slightly visible on the right-hand edge of the scene. The water depth in the vicinity of this shoal was computed to be 8.3 ft, or nearly 1 1/2 fathoms. The navigation charts for this area show depths which range from 1 3/4 to 3 fathoms at this point (C and GS 901) (see Fig. 11).

We were very fortunate in this instance because a single, well defined wave set with fairly long wave length was moving directly onto a known shoal area. This resulted in transforms which afforded simple and highly informative measurement and interpretation.

2.3.4. PUERTO RICO, PUNTA GUAYANILLA AREA

The fourth test site, centered near a rocky shoal area just west of the harbor entrance to Guayanilla, is shown in Fig. 12. The navigation charts for this harbor show shoal depths from 10 to 25 ft (1 3/4 to 4 fathoms), although this range might vary somewhat with tide level. The deep-

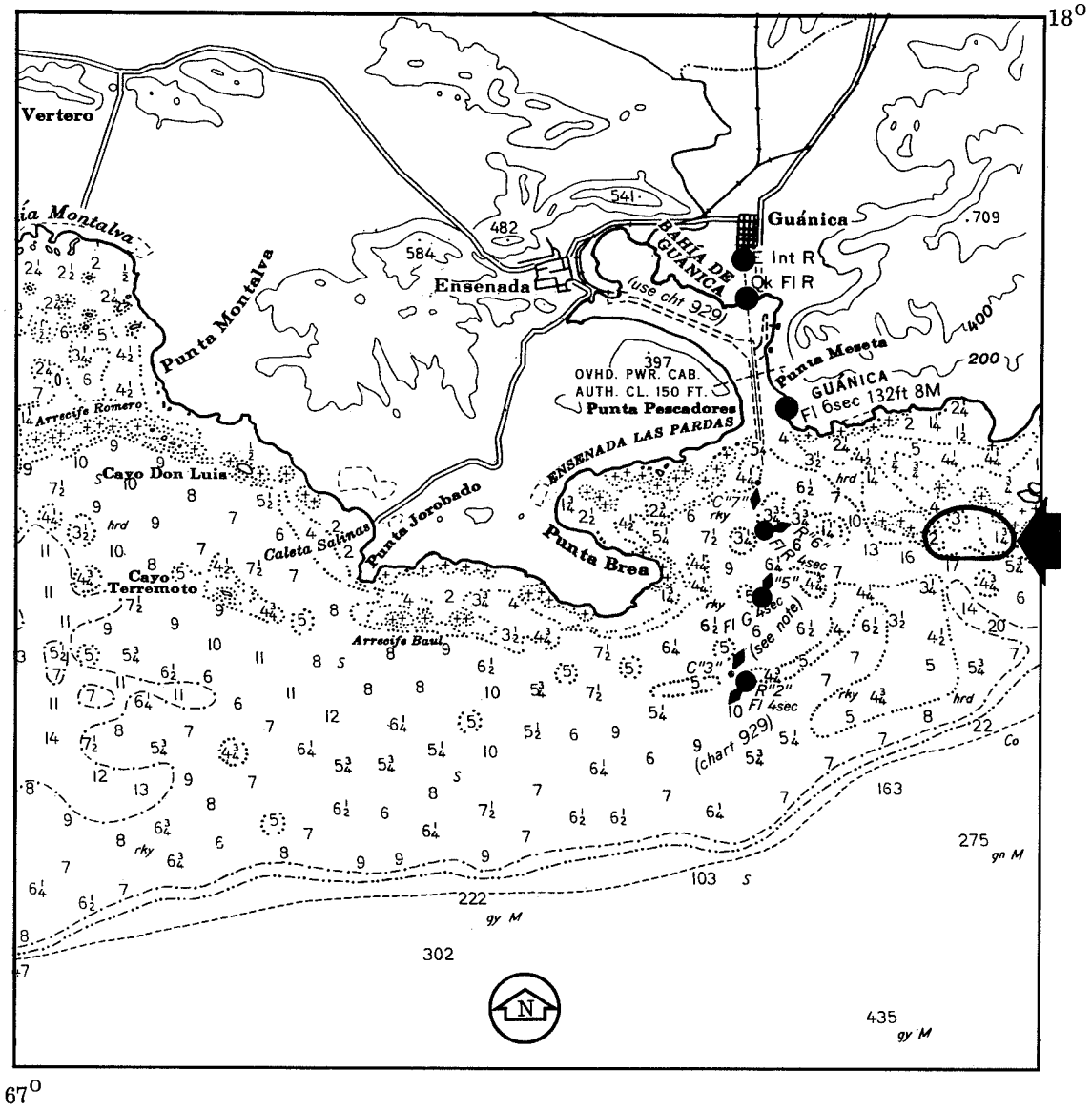

FIGURE 11. WEST COAST OF PUERTO RICO

water wave length here measured 164 ft, which is quite close to the deep-water wave length measured off Punta Brea. Both areas were photographed within minutes of each other.*

In this test, we photographed shallow-water wave transforms at two different positions. The shoal area farthest from shore (B) had a computed depth of 13 ft, which was reduced to 8 ft when

* The reduced prints and transforms for these two sites along the south coast of Puerto Rico were photographed directly from the Ansco D-500 film.

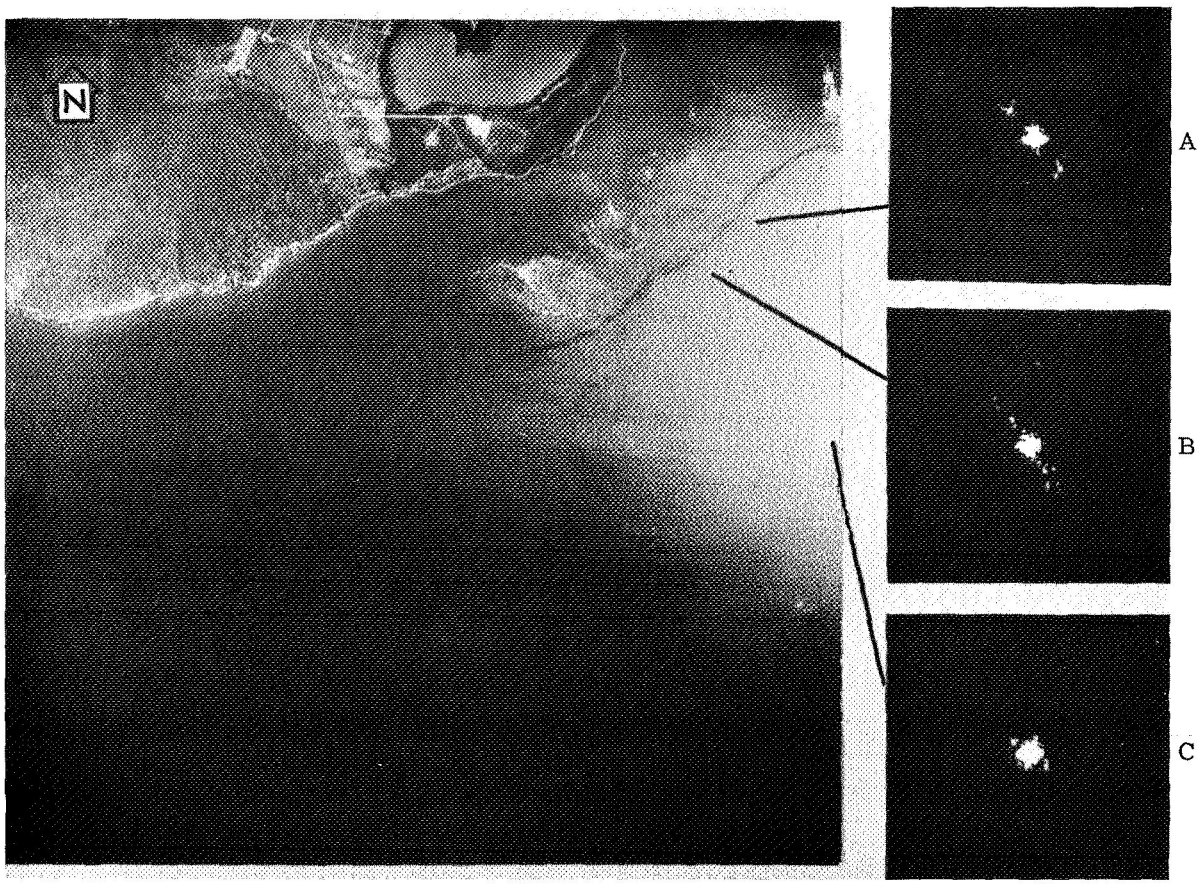

FIGURE 12. WATER-DEPTH MEASUREMENT OFF PUNTA GUAYANILLA, PUERTO RICO

measured closer to shore (A). The wave set transformed at A has been repeated toward the northwest, from point B, as the friction of the shoal area bends the wave set in its advance toward shore.

2.3.5. LAKE MICHIGAN

The Lake Michigan test site near Big Sable Point, Michigan was the fifth area studied. It was selected because of our desire to demonstrate the use of optical transform techniques on very high altitude imagery. The scene pictured in Fig. 13 is part of the NASA flight imagery collected at an altitude of 60,000 ft on Mission No. 103 during the summer of 1969.

The deep-water transform in Fig. 13 (A) displays two wave sets. The most obvious set, moving onshore from a westerly direction, measured approximately 73 ft in length. A second wave set can be seen on a north-south axis. While this set is not as distinct in the transform, it is quite obvious in the photograph; it is approximately 115 ft long.

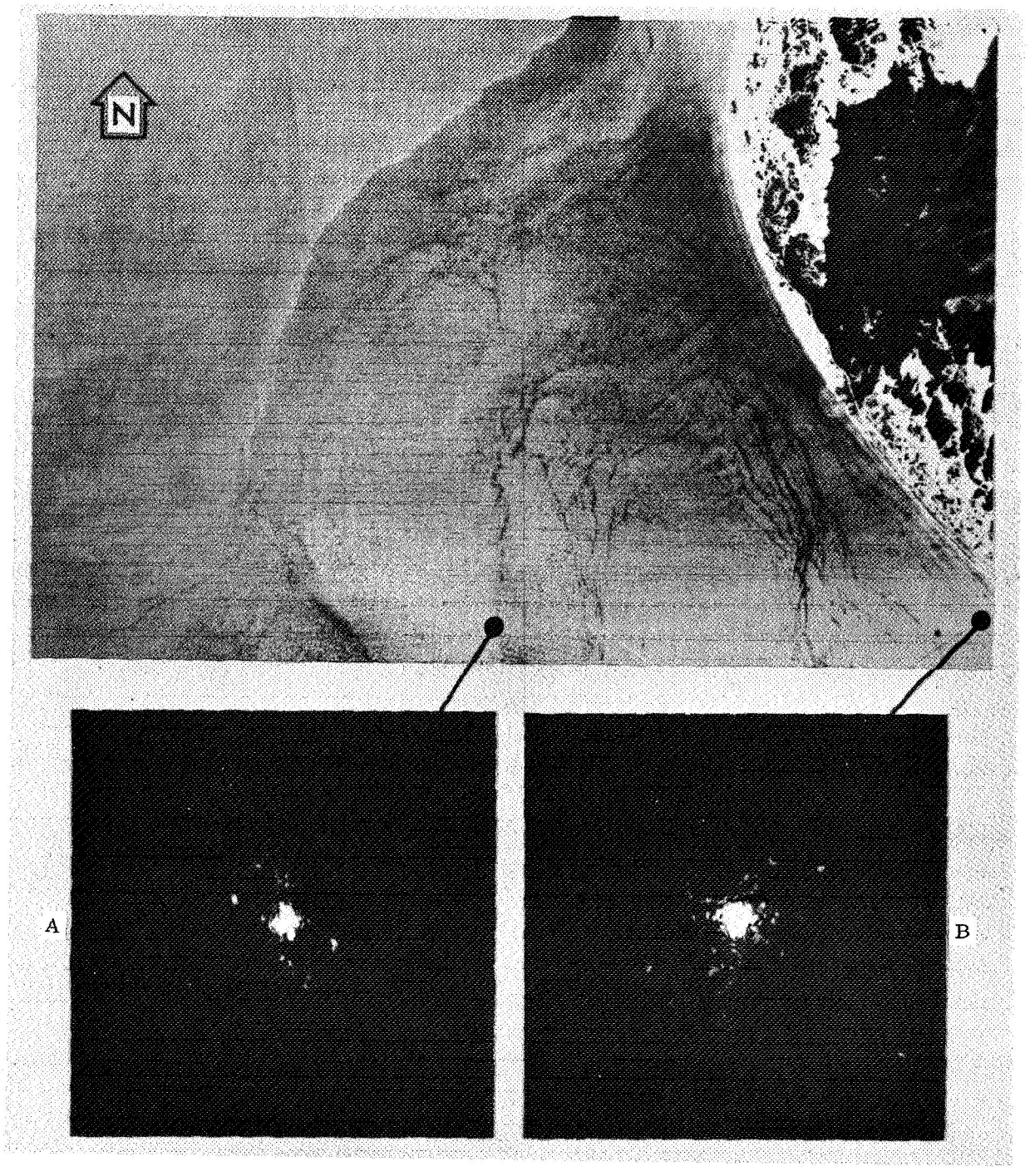

FIGURE 13. WATER-DEPTH MEASUREMENT NEAR BIG SABLE POINT, LAKE MICHIGAN

The shallow-water transform shows a very distinct high-frequency component which is moving northeast toward the shore. We verified its wave length, computed to be 40 ft, by counting the waves in the imagery and equating their number with the imagery scale.

In this test it was not clear where the shallow-water wave set apparent in transform B originated. Therefore, it was difficult to compute a shallow depth. On the day the imagery was collected, the current was moving south, while the prevailing wind was blowing in a northerly direction. The information in the reflected sun-glitter pattern is not sufficient for us to determine the origins of all the wave sets depicted in the transform. These conditions represent a constraint on interpretation when we are limited to single, reflected, sun-glitter pattern. Yet with such small scale photography, the facts that dominant wave sets were identified and that transform measurements were verified by an actual wave count are encouraging.

2.4. DISCUSSION OF RESULTS

Optical Fourier analysis of photography can produce valuable information concerning both sea-state characteristics and wave-refraction phenomena. We have demonstrated the advantages of processing imagery dominated by a single, well-defined wave set and some of the problems associated with more complex wave forms. The application of optical Fourier analysis to very long wave lengths is supported by the fact that depth determination is directly related to the original deep-water wave length and greater depths can be measured by this method than can be measured by light-penetration methods.

In particular, we were successful in computing depths from high-altitude imagery (20,000 ft and above), where the high-frequency wind waves are less likely to be imaged on top of the lower frequency wave sets. The presence of the higher frequency components increases the problem of interpretation. The use of an apodizing filter, however, proved to be very effective in simplifying the transform, and thus made measurements and interpretation much more exact.

It is therefore obvious that, for present techniques to be successful, interpretors are needed to make specific decisions about the transform relative to particular wave sets in the image scene. It is difficult at present to conceive of an automated system which would provide all the necessary interpretation. However, an automated system could greatly increase the interrogation speed of imagery in order to help locate the most promising areas for further analysis (a procedure which is both lengthy and costly at present).

3
DETERMINATION OF WATER DEPTH BY USE OF REMOTELY SENSED MULTISPECTRAL DATA

3.1. GENERAL CONSIDERATIONS

A remote sensor oriented toward a shallow body of water receives electromagnetic radiation from sunlight scattered by the water and atmosphere and from sunlight reflected from the ocean floor and the air-water interface. Because that portion which has been reflected from the ocean floor must pass through an intervening, absorbing water layer, the power received by the sensor will be dependent upon the extent of the attenuation and, thus, upon the depth of the water.

Quantitatively, this process can be described essentially by the following relationship:

$$P(\Delta\lambda) = \int_{\lambda}^{\lambda+\Delta\lambda} \left[\rho(\lambda)L_{\lambda}e^{-(\sec\theta+\sec\phi)\alpha(\lambda)Z} + \rho(\lambda)_{a/w}L_{\lambda}\right] d\lambda + P(\Delta\lambda)_{sc} \qquad (1)$$

where $P(\Delta\lambda)$ = the power received in the spectral band

$P(\Delta\lambda)_{sc}$ = the scattered sunlight

$L(\lambda)$ = the incident solar spectral radiance

$\rho(\lambda)$ = the bottom reflectance

$\rho(\lambda)_{a/w}$ = the air-water interface reflectance

$\alpha(\lambda)$ = the water's attenuation coefficient

θ = the viewing angle (from the nadir)

ϕ = the solar-illumination angle (from the vertical)

Z = the water depth

For very deep water, the exponential term of Eq. (1) goes to 0, and yields the following deep-water expression:

$$\lim_{Z\to\infty}[P(\Delta\lambda)] = \int_{\lambda}^{\lambda+\Delta\lambda} \rho(\lambda)_{a/w}L_{\lambda}\,d\lambda + P(\Delta\lambda)_{sc} = P(\Delta\lambda)_{\infty} \qquad (2)$$

Although the light scattered by the water will increase with depth, the effect is slight. Thus, combining Eqs. (1) and (2) we obtain

$$P(\Delta\lambda) - P(\Delta\lambda)_{\infty} = \int_{\lambda}^{\lambda+\Delta\lambda} \left[\rho(\lambda)L_{\lambda}e^{-(\sec\theta+\sec\phi)\alpha(\lambda)Z}\right] d\lambda \qquad (3)$$

On the assumption that both P and P_{∞} can be measured, Eq. (3) enables us to calculate water depth. In practice, P_{∞} is determined when we scan over very deep water. By averaging the signal over many scan lines for each spectral band, we obtain P_{∞} as a function of the scan angle (θ) and the spectral band. This function is then subtracted from the shallow-water signal (also a function of θ and λ) and leaves, to a first approximation, only the bottom-reflection term.

The signals at the output of the remote sensors are not, of course, power but are proportional to the incident power:

$$V_i = K_i P_i \tag{4}$$

where V_i is the signal from the i-th spectral channel, K_i is a proportionality constant, and P_i is the incident power. Since the K_i's cannot be known a priori, they are determined by scanning over a sun sensor (ss) illuminated by the same radiance as the scene, which has known spectral properties:

$$(V_i)_{ss} = K_i (P_i)_{ss} \tag{5}$$

The power incident upon the sun sensor is:

$$(P_i)_{ss} = \int_{\lambda}^{\lambda+\Delta\lambda} [\rho(\lambda)_i]_{ss} L_\lambda \, d\lambda \tag{6}$$

where $[\rho(\lambda)_i]_{ss}$ is the throughput of the sun sensor in the i-th spectral channel. Substituting Eq. (5) into (4), the following is obtained:

$$V_i = \left(\frac{V_i}{P_i}\right)_{ss} P_i \tag{7}$$

If narrow spectral bands are assumed, Eqs. (3) and (6) can be reduced:

$$P(\Delta\lambda) - P(\Delta\lambda)_\infty = \rho(\lambda) e^{-(\sec\theta + \sec\phi)\alpha(\lambda)Z} L_\lambda \Delta\lambda$$

$$(P)_{ss} = [\rho(\lambda)]_{ss} L_\lambda \Delta\lambda$$

Substituting these two expressions into Eq. (7), we obtain:

$$\Delta V_i = \left(\frac{V_i}{\rho(\lambda)}\right)_{ss} \rho(\lambda) e^{-(\sec\theta + \sec\phi)\alpha(\lambda)Z} \tag{8}$$

where ΔV_i is the differerence of the shallow- and deep-water signals in the i-th spectral channel.

In general, we are not sure enough of the accuracy of $\rho(\lambda)$ and $\alpha(\lambda)$ to have a reasonably exact solution to Eq. (8). It can be shown that ratios of the signals from pairs of spectral channels lead to more reliability, as follows:

$$\frac{\Delta V_i}{\Delta V_j} = \frac{[V_i/\rho(\lambda_i)]_{ss}}{[V_j/\rho(\lambda_j)]_{ss}} \frac{\rho(\lambda_i)}{\rho(\lambda_j)} e^{-(\sec\theta + \sec\phi)(\alpha_i - \alpha_j)Z} \tag{9}$$

This expression is very useful because, while ρ and α may not be known exactly, their ratios and differences (respectively) are known to a high degree of accuracy.

This latter conclusion can be demonstrated with an example. Figure 14 shows the ratios of reflectance for four selected bottom types as they were sensed by a scanner which has the following spectral bands:

Channel	Wavelength Bands (μm)
1	0.45-0.47
2	0.47-0.48
3	0.50-0.52
4	0.52-0.55
5	0.55-0.58
6	0.58-0.63
7	0.63-0.68
8	0.75-0.85

(The eighth channel is essentially opaque for water and is used only to test for above-surface objects.)

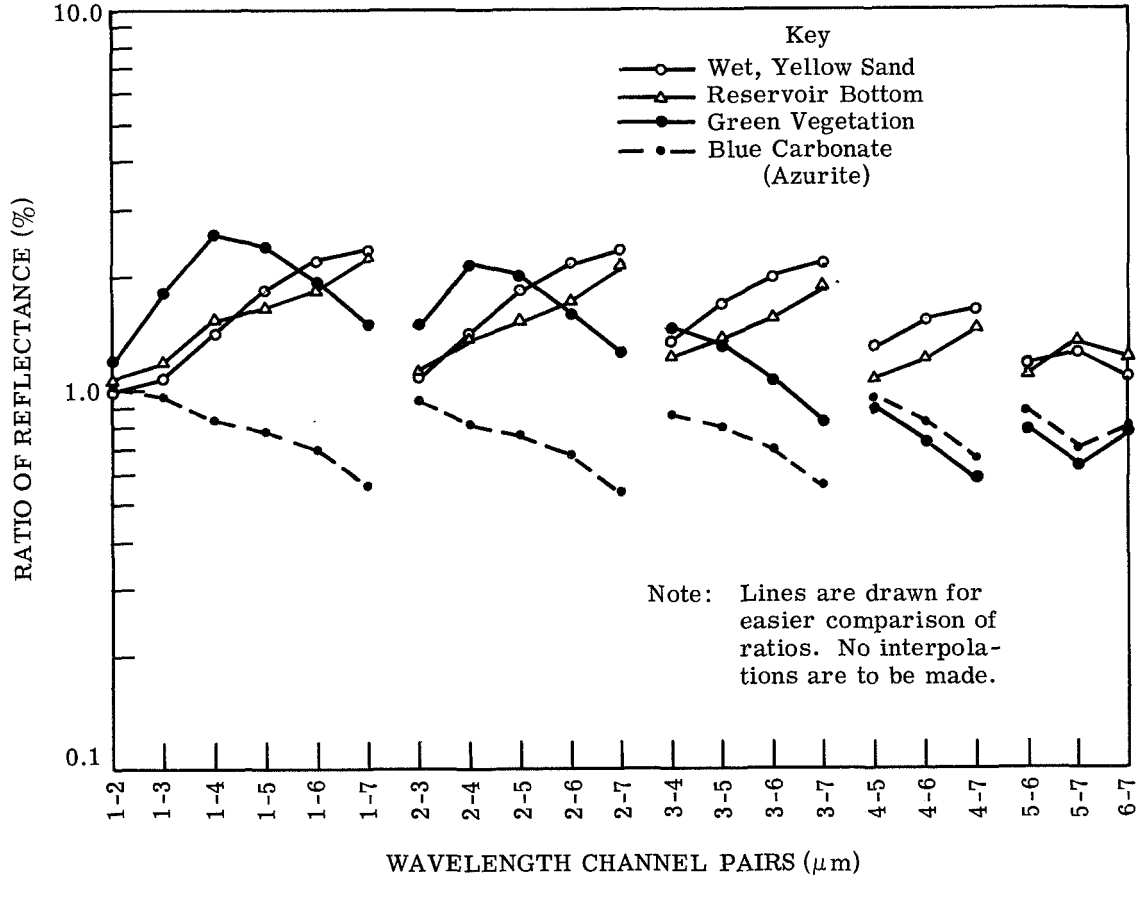

FIGURE 14. RATIOS OF REFLECTANCE IN CHANNEL PAIRS FOR FOUR SELECTED BOTTOM TYPES

The bottoms selected were chosen on the basis of their generality (in the case of the sands and vegetation) or in the case of the blue carbonite (azurite) on the basis of the improbability of their occurrence. The latter was used to demonstrate that even an unlikely bottom will work, if there is judicious choice of channel pairs.

The criterion for acceptable spectral channel pairs was that the reflectance ratios should be as similar as possible for all bottoms. Including the unlikely azurite bottom, the choices are:

Channel Pair	Variation In Reflectance Ratios (%)
1-2	±10
4-5	±20
5-6	±22
2-3, 6-7	±25
3-4	±30
1-3	±37
3-5, 4-5, 5-7	±45

The remaining pairs have variations ranging from ±65% to ±110%. If we exclude the azurite, the choices become:

Channel Pair	Variation In Reflectance Ratios (%)
1-2, 1-6, 3-4	±10
2-5, 3-5	±15
2-3, 2-6	±18
1-5, 4-5	±21
5-6	±23

Variations in the remaining pairs range from ±26% to ±67%.

A further criterion for the choice of channel pairs is the requirement that the α differences must be relatively independent of water type and turbidity. Figure 15 is a plot of the attenuation differences for three selected oceanic and coastal water types. Data from the Chesapeake Bay are added for comparison. (The effects of silt suspended in the water are ignored for the present, but will be discussed later.) As can be seen readily by an inspection of Fig. 15, very few optimum pairs exist. To demonstrate, consider first Eq. (9) when solved for Z.

$$Z = \frac{1}{f(\theta, \phi)(\alpha_j - \alpha_i)} \ln \left\{ \frac{\Delta V_i}{\Delta V_j} * \frac{[V_j/\rho(\lambda_j)]_{ss}}{[V_i/\rho(\lambda_i)]_{ss}} * \frac{\rho(\lambda_j)}{\rho(\lambda_i)} \right\} \qquad (10)$$

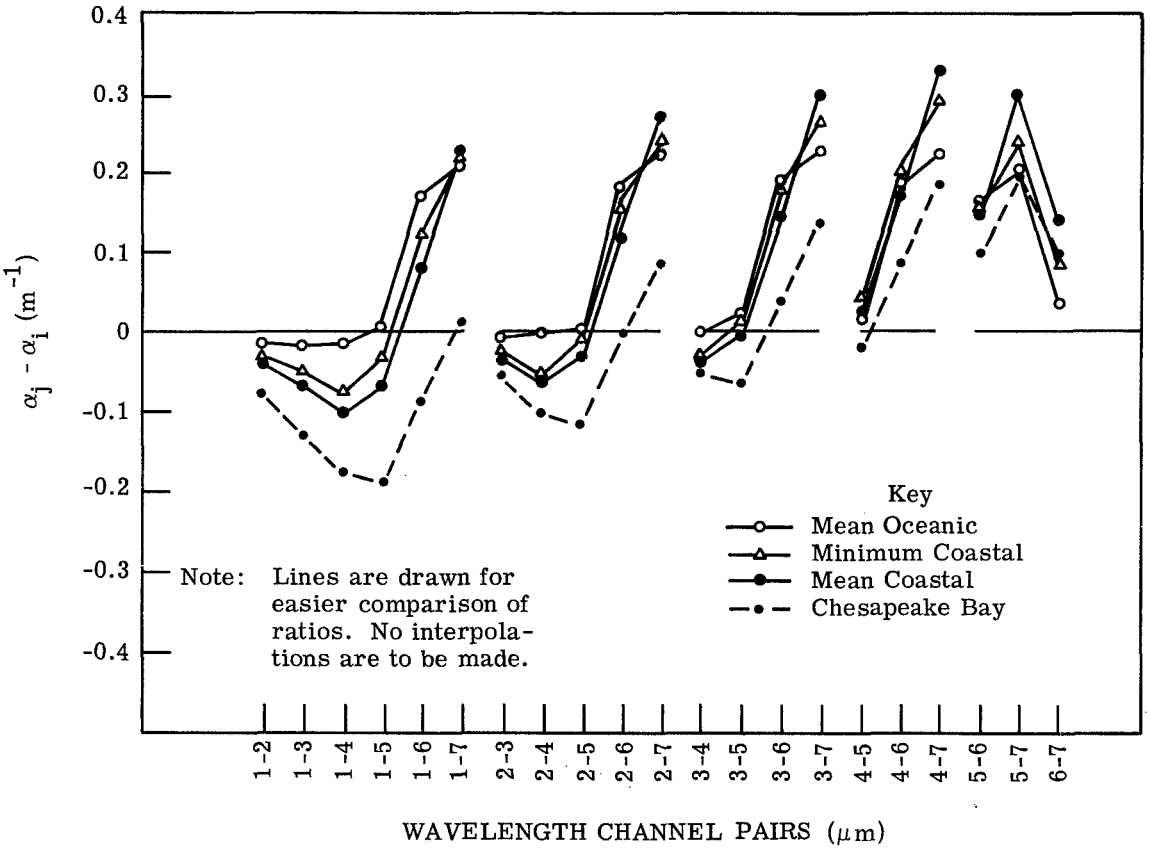

FIGURE 15. DIFFERENCES IN WATER-ATTENUATION COEFFICIENTS FOR CHANNEL PAIRS

Note that a change of sign in $(\alpha_j - \alpha_i)$ will change the sign of Z. Also, the smaller the $(\alpha_j - \alpha_i)$, the greater will be the error in Z for a given error in the signal levels and/or reflectance ratios. The criteria for acceptable $(\alpha_j - \alpha_i)$'s, then, are (1) common sign and (2) fairly large magnitude.

For all four kinds of water, the most acceptable channel pairs are:

Channel Pair	Variation In $(a_j - a_i)$ (%)
5-7	±22
5-6	±27
4-7	±33
3-7	±46
4-6	±52
2-7	±80
6-7	±92

The other pairs have variations which range from ±120% to ±600%.

Excluding the Chesapeake Bay data from consideration, the best pairs are:

Channel Pair	Variation In $(a_j - a_i)$ (%)
1-7	±4
4-6, 5-6	±5
2-7	±9
3-7	±13
4-7, 5-7	±20
2-6	±24
3-6	±30
1-6, 4-5	±45

Variations from ±90% to ±160% occur in the remaining pairs.

Comparison of these results with those obtained from bottom reflectance considerations reveals very little overlap. Those channels most acceptable from one consideration are, in general, least acceptable from the other. Only three exceptions occur—channel pairs 2-6, 4-5, and 5-6. Taking a combination of the two types of errors described above, we might expect the following variations:

Channel Pair	Total Variation (%)
5-6	±14
2-6	±21
4-5	±32

We obtain the final results of depth measurements by computing depths (using the acceptable channel pairs) and taking the mean. Weighting could be done to diminish the effect of the least reliable channel pairs on the final measurements.

3.2. DEMONSTRATION OF REMOTE MEASUREMENT OF DEPTH FOR A LAKE MICHIGAN BEACH AREA

Data available over Lake Michigan's shoreline near Bridgeman, Michigan provided an excellent opportunity to measure water depths by the multispectral ratio method but under somewhat different conditions than those encountered in the reef areas in the Florida Keys.

The beach and lake bottom on the east side of the lake consists almost entirely of fine silica sand, and the bottom, in general, slopes away gradually to depths of 70 ft at about 2 1/4 miles offshore. Shifting sandbars appear frequently within the first several hundred feet from shore, but the changes in depth are never abrupt. Because of the uniform nature of the sandy bottom,

it was felt that any one of several combinations of wavelength channels in the visible region could be used to give accurate depth measurements and, simultaneously, to provide enough data for an analysis of the limitations of each set of channels. Unfortunately, no laboratory data on water absorption and silica sand which specifically applied to the Lake Michigan area were available; thus, only closely approximating data could be used in the depth equation. We assumed bottom reflectances and water-attenuation coefficients like those shown in Figs. 16 and 17, and

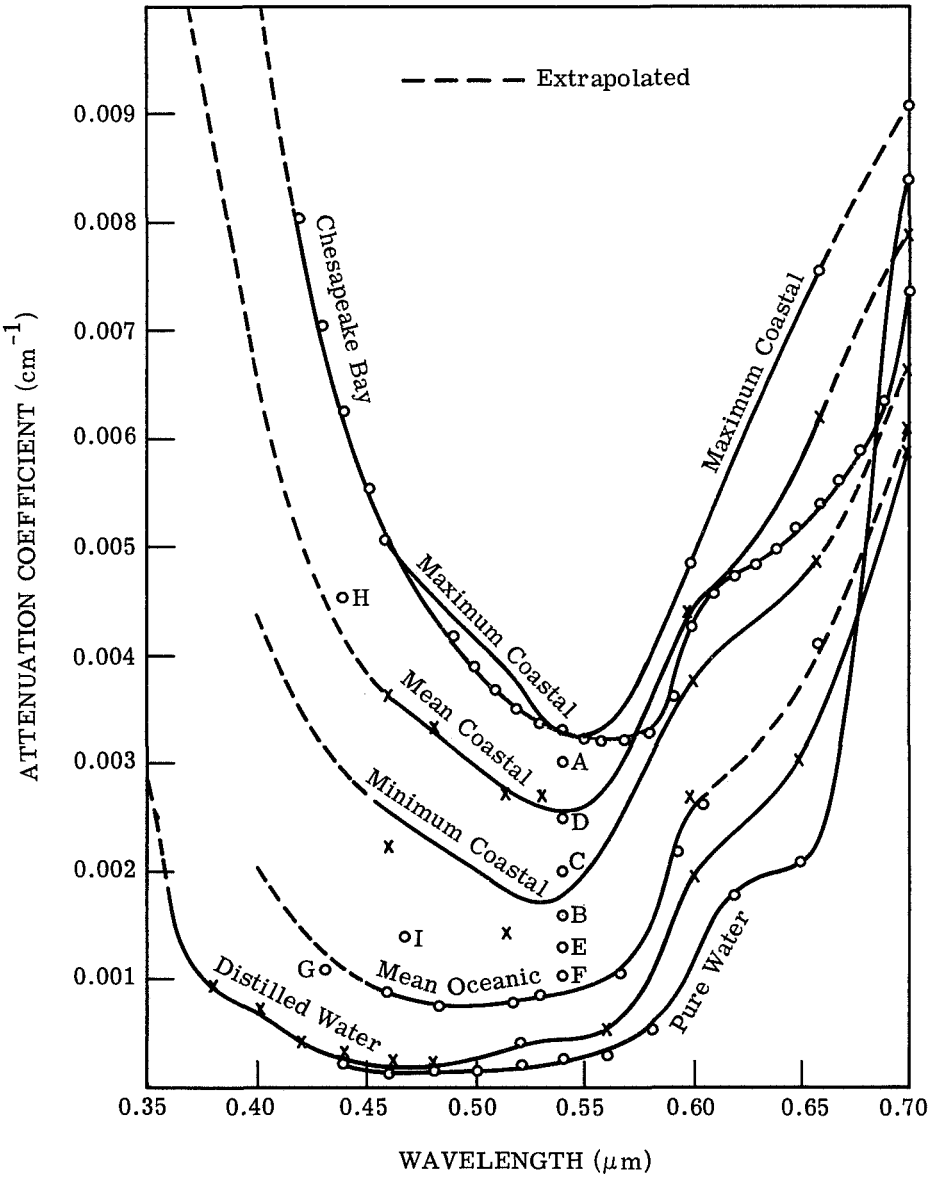

FIGURE 16. ATTENUATION COEFFICIENT VERSUS WAVELENGTH FOR PURE WATER AND SEA WATER

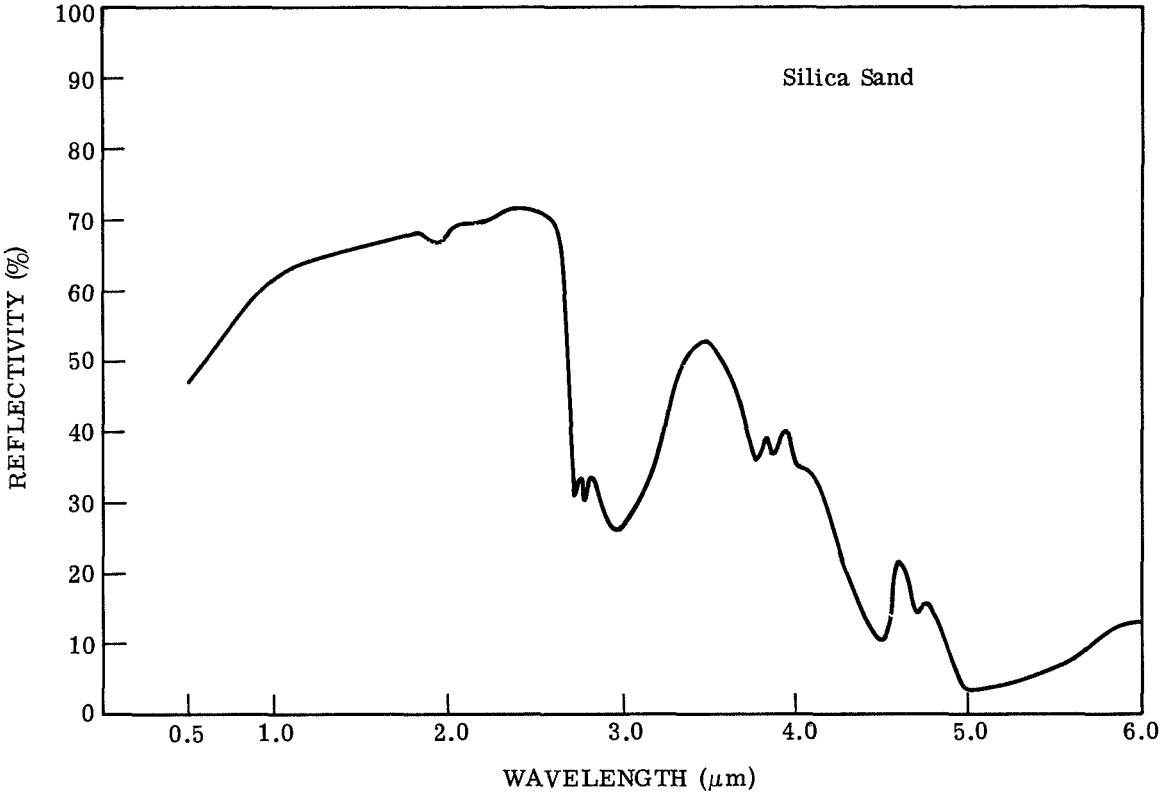

FIGURE 17. REFLECTANCE OF SILICA SAND

(at a point about ten miles south of Benton Harbor, Michigan) depths were calculated for two flight lines perpendicular to shore and separated by several hundred feet.

When the first three combinations of channels failed to give reasonable depths according to recent depth charts for the area, the fault was placed on the assumed bottom reflectances and water-attenuation coefficients. In view of this problem, we reversed the procedure and used digitized multispectral scanner outputs and known depths obtained from fathometer data over the flightline to solve the depth equation for the water and sand parameters.

Initially, we did this by picking two points along the flight path, one corresponding to a known shallow depth and the other to a deep depth, and, by trial and error, working backwards from the depth equation to reach the relative values of α_λ and ρ_λ, which gave the correct depth at these points. These derived parameters are relative values because the depth equation uses only the difference between attenuation coefficients and the ratios of bottom reflectance. The particular values achieved, shown in Table 1, were based on an assumed α at 0.655 μm of 0.063 (ft^{-1}) and a ρ at 0.655 μm of 43%. Later on, an exact relation which gave the relative attenuation coefficients and bottom reflectances directly from the multispectral voltage ratios was obtained from the

TABLE 1. CALCULATED VALUES FOR ATTENUATION COEFFICIENT AND BOTTOM REFLECTANCE

Bandpass (μm)	$\alpha(-1)$	$\rho(\%)$
0.62 - 0.69	0.0630	43.0
0.57 - 0.62	0.0573	40.5
0.55 - 0.57	0.0525	34.0

depth equation. The values derived from this method agreed almost exactly with those arrived at earlier.

By applying these generated parameters to all points along the flightline, we can obtain a profile of water depth. The results of this procedure are shown in Fig. 18, where depth calculations for the three combinations of wavelengths (0.545-0.575 μm, 0.575-0.62 μm, and 0.62-0.69 μm) are compared to the approximate actual depths given on the depth charts. In Fig. 19, the average of these three depth calculations is plotted. The agreement, in general, is quite good. However, beyond 15 ft, system noise starts causing large variations in depth, and, therefore, depths greater than 25 ft could not be determined with this particular data set. The dotted portion of the actual depth curve shows the region of a shifting sandbar which, apparently, was not very pronounced at the time of the overflight.

When these values were put into the depth program in order to develop a digital depth map of the area, the resulting depths were not as uniform as expected, especially those perpendicular to the shoreline. The variation across a scanline was no doubt the result of the rough wave action and sun glitter at the water's surface. To help remove the effect, a moving-window procedure was employed to average scanner voltages over rectangles of water 60 ft × 6 ft. The center of each successive rectangle was displaced by 3 ft. The overall result was a degrading of the resolution into overlapping 60 ft × 6 ft rectangles. The beach gradient derived from this smoothed data (Fig. 20) is the average of the output from three combinations of wavelengths (like those in Fig. 19). The white strip at the left of the picture is a cofferdam which juts out into the water and marks the land-water boundary. The dark rectangles appearing throughout the map are caused by noise spikes, which result in erroneous voltage ratios and, hence, poor depth calculations. The strip shown is about 700 ft long.

When the equation was reversed and when known depths were used, we encountered difficulty generating water-attenuation coefficients and bottom reflectances because we assumed (1) that the water attenuation did not change along the flight path and (2) that depth measurements of 25-30 ft were obtainable without forcing the data to yield results inconsistent with the actual physical properties of the water and bottom. Figure 21 shows water-depth calculations for the same three combinations of channels shown in Fig. 18, but the water-attenuation coefficient and bottom

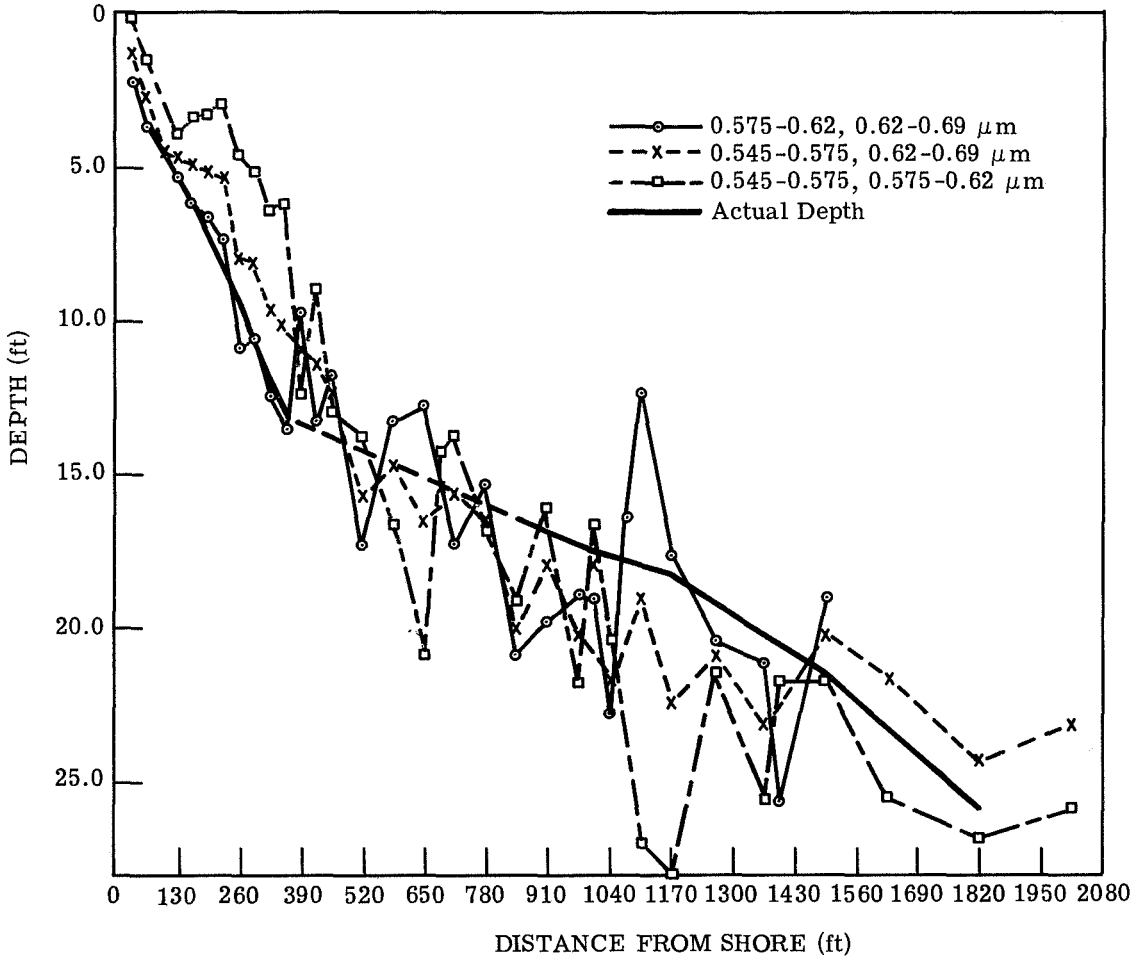

FIGURE 18. DEPTH CALCULATIONS FOR THREE COMBINATIONS OF WAVELENGTH

reflectances are generated from data corresponding only to depths of 13 ft and to distances of 300-400 ft offshore, instead of depths of 26 ft and distances of 2000 ft offshore. The values of attenuation coefficents and bottom reflectances achieved are shown in Table 2. As can be seen from Fig. 21, the agreement is excellent for the shallower areas but very poor for deeper areas, especially those in the sets of channels in which the difference in attenuation coefficients is small.

Other wavelengths in the blue region (0.45 μm to 0.47 μm) were also combined to reach depths up to 13 ft. The improved accuracy resulted when the water-attenuation and bottom-reflectance curves shown in Figs. 22 and 23 were used in the calculations. A comparison of these curves with those in Figs. 16 and 17 shows that although the general shape is similar, neither the bottom reflectance nor the water attenuation in the considered area can be classified as typical;

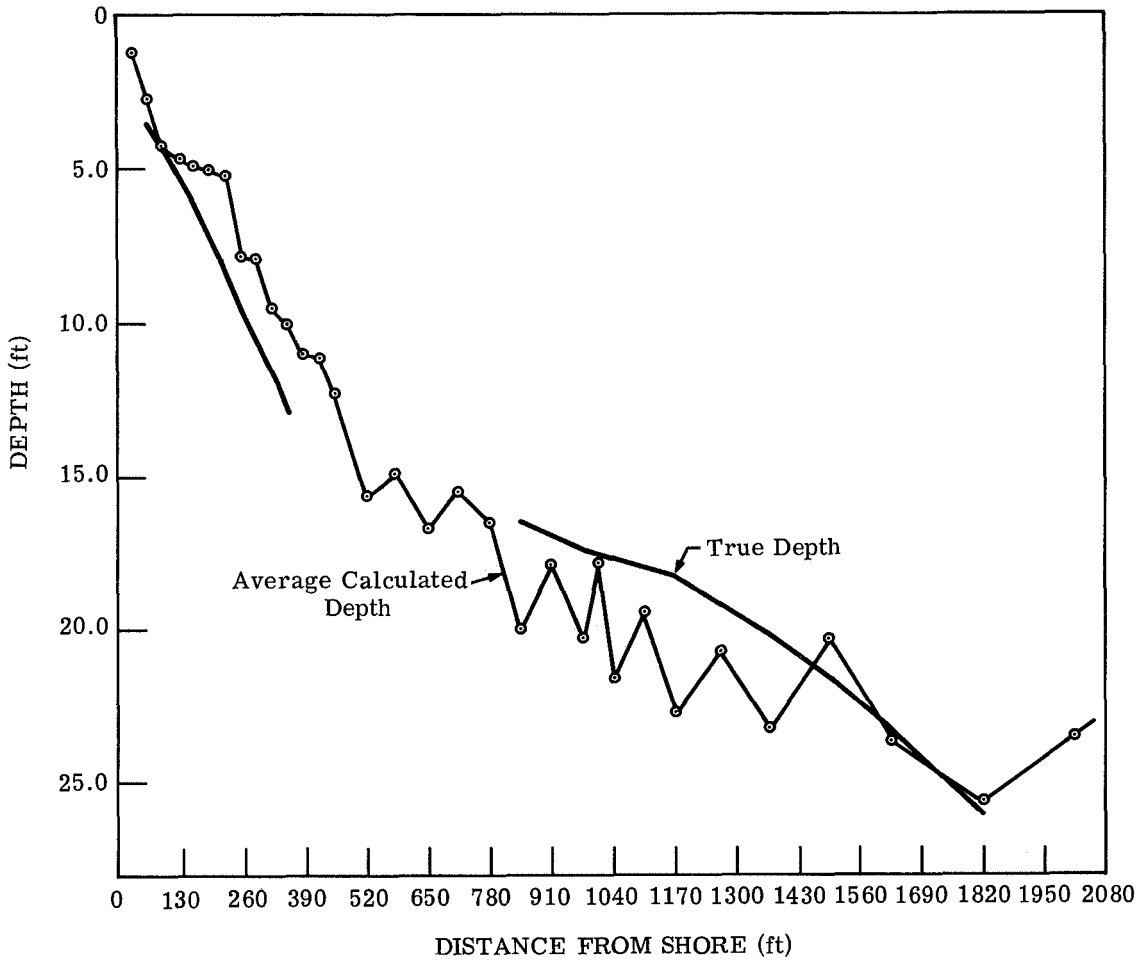

FIGURE 19. AVERAGE OF THREE DEPTHS VERSUS DISTANCE FROM SHORE

TABLE 2. VALUES CALCULATED FROM NEAR-SHORE DATA ONLY FOR ATTENUATION COEFFICIENTS AND BOTTOM REFLECTANCES

Bandpass (μm)	α(ft-1)	ρ(%)
0.62 - 0.69	0.0630	43.0
0.57 - 0.62	0.0570	40.5
0.55 - 0.57	0.0546	33.9

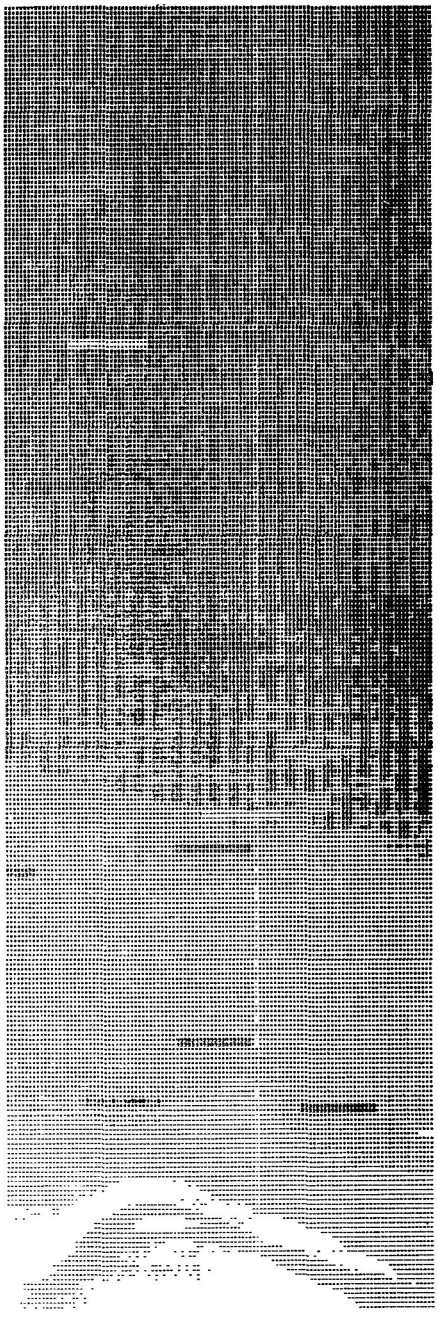

FIGURE 20. COMPUTER-GENERATED CHART OF WATER DEPTH NEAR BRIDGEMAN, MICHIGAN

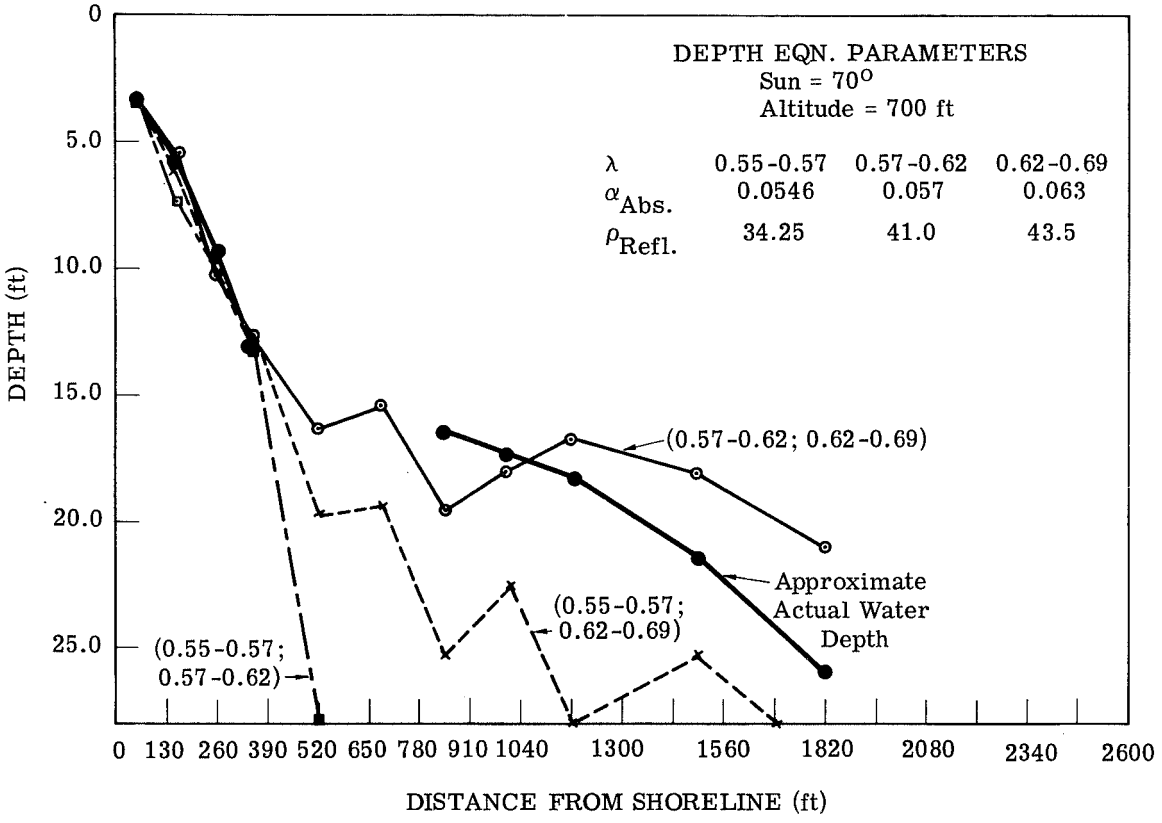

FIGURE 21. LAKE MICHIGAN WATER-DEPTH CURVES GENERATED FROM SHALLOW, TURBID WATER PARAMETERS

therefore, neither one can be generalized. Table 3 gives the actual depth which we calculated by combining the six wavelength regions available in the different possible combinations of two channels and by using the data shown in Figs. 22 and 23. Combinations of channels in which the difference in attenuation ($\Delta\alpha$) is small (e. g., 0.52-0.55; 0.55-0.57) are not very useful for determining depths. Usually, close agreement with approximate actual depths was achieved up to 13 ft, although a need for added gain and/or smoothing is apparent. Beyond 13 ft, variations in depth measured with the majority of channels (especially the blue region) indicated that the calculated attenuation coefficient and bottom reflectance in Figs. 22 and 23 were not correct for the deeper waters.

Thus, if the data are forced to give correct depth to 25-30 ft, the shallow-water calculations reached with the red channels will be erroneous; the blue channels will yield completely false

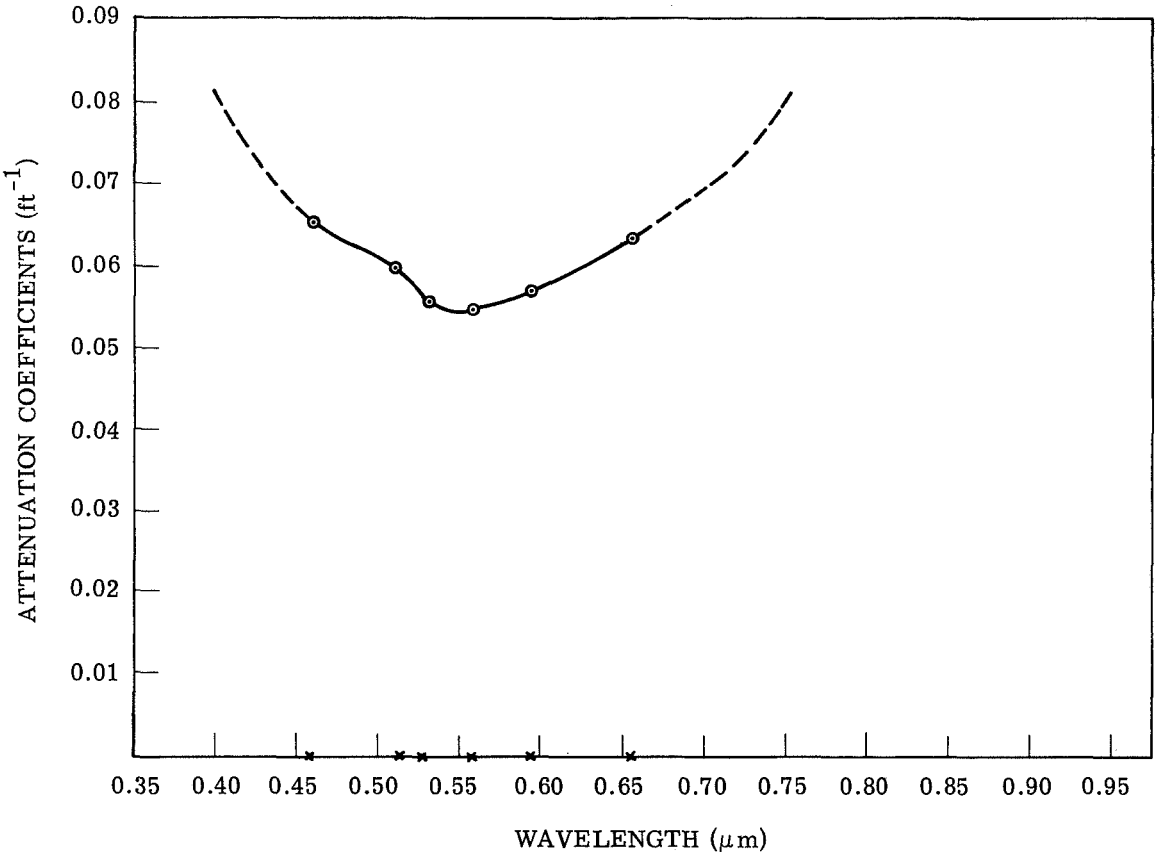

FIGURE 22. WATER-ATTENUATION COEFFICIENT (LAKE MICHIGAN) GENERATED FROM DEPTH EQUATION

results. Evidently, the shallower water (perhaps because of suspended particulate matter such as sand) has a scattering effect which cannot be ignored, even in the red region.*

In the discussion just presented, the need for more specific laboratory data on water attenuation and bottom reflectances is illustrated, since it is obvious that for this particular data set generalized values of α and ρ will not yield correct depths. Also, we should know what the limitations are on the multispectral voltage-ratio technique for measuring depths. Until an accurate picture of the actual water attenuation and bottom reflectance is achieved, one can

*One potential use for the information given above might be in the development of a technique whereby turbidity could be measured from airplane or satellite altitudes. Of course, in the development of such a technique it is necessary to know the actual depth. Therefore, the installation of a laser-depth measuring system on board an aircraft becomes very important, if we are to get an independent depth measurement.

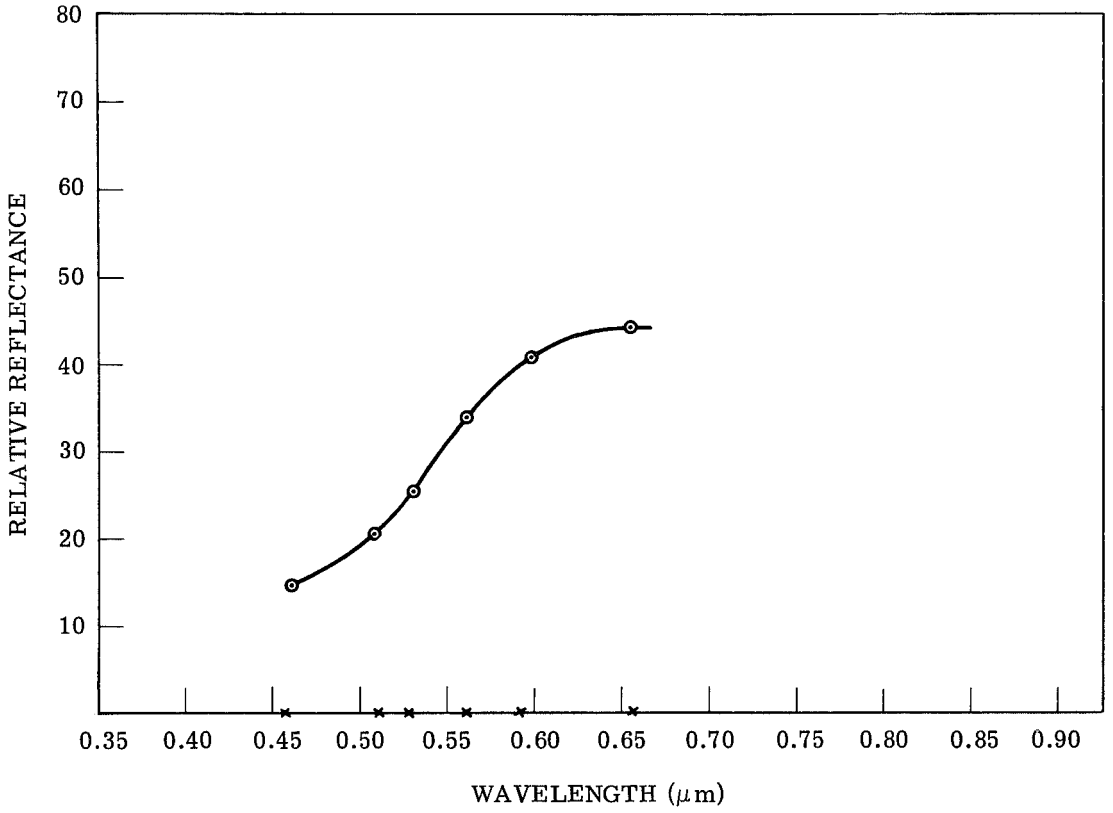

FIGURE 23. RELATIVE BOTTOM-REFLECTANCE OF LAKE MICHIGAN SILICA SAND

only hypothesize that the curves shown in Figs. 22 and 23 are correct and that the depth equation gives reasonable accuracy to depths of 25-30 ft. More information is required if one is to determine whether these empirically derived values do agree with laboratory data and, if not, why they give reasonable depth calculations.

3.3. APPLICATION OF MULTISPECTRAL TECHNIQUES TO CAESAR CREEK/AJAX REEF AREA, MIAMI, FLORIDA

Multispectral data, collected over the Caeser Creek/Ajax Reef area off Miami, during 10 March 1970, was processed using the ratio techniques described earlier in this section. Little in the way of ground-truth data was available, with the exception of some existing depth charts.

A few generalizations can be made about the study area. First, the most obvious feature is Caesar Creek itself, which starts at Old Rhodes Key and Christmas Point and extends generally eastward, toward the Ajax and Pacific Reefs. Water depths in the Creek are from 10-20 ft, with north and south banks as shallow as 1 ft.

TABLE 3. DEPTHS CALCULATED FROM VARIOUS SPECTRAL CHANNEL PAIRS

Wavelength Regions	Depths 65 ft	97 ft	160 ft	195 ft	227 ft	260 ft	325 ft	357 ft
0.57-0.62; 0.62-0.69	3.7	4.3	6.1	6.5	7.3	10.9	12.4	13.5
0.55-0.57; 0.62-0.69	3.3	5.4	5.9	6.2	6.4	9.7	11.7	12.3
0.55-0.57; 0.57-0.62	2.3	7.5	5.5	5.3	4.7	7.3	10.3	9.9
0.52-0.55; 0.62-0.69	3.3	3.8	4.8	3.6	5.8	9.7	10.7	12.5
0.52-0.55; 0.57-0.62	2.1	2.5	1.4	-4.0	2.0	6.6	6.3	9.9
0.52-0.55; 0.55-0.57	3.3	24.2	18.9	36.0	13.7	9.7	23.6	9.9
0.50-0.52; 0.62-0.69	3.0	6.2	0.3	-0.5	-2.6	7.4	7.5	14.3
0.50-0.52; 0.57-0.62	3.5	2.2	11.2	14.3	18.1	14.7	17.9	12.5
0.50-0.52; 0.55-0.57	3.0	5.1	8.9	9.7	11.2	10.9	13.6	11.2
0.50-0.52; 0.52-0.55	2.8	2.3	7.3	5.8	10.7	10.9	12.5	11.3
0.45-0.47; 0.62-0.69	2.3	0.4	19.8	28.8	18.7	11.2	39.0	8.5
0.45-0.47; 0.57-0.62	3.2	3.2	9.5	12.2	10.1	10.8	19.3	12.1
0.45-0.47; 0.55-0.57	3.0	4.4	8.4	10.3	8.6	9.9	16.7	11.5
0.45-0.47; 0.52-0.55	3.0	3.1	7.7	8.5	8.3	9.9	16.3	11.6
0.45-0.47; 0.50-0.52	3.2	3.8	8.1	11.2	5.9	8.9	20.1	12.0
Average*	3.1	4.4	7.1	7.8	7.9	9.9	12.9	11.5
Actual Depth	3.5	4.5	6.5	7.0	8.5	9.5	12.0	13.0

*Average does not include obvious errors resulting from noise.

Second, there are some fairly obvious shoals (or reefs) along the flight line from Caesar Creek to Ajax Reef (Fig. 24, with depths which range from 2-16 ft; these are surrounded by water about 24-32 ft deep. Third, Ajax Reef itself, with a depth of 3-16 ft, is followed by a sudden dropoff to 300 ft.

Figure 25 (color map of 6500-ft data) is a computer-generated depth map color-keyed to depth. The dark green areas (upper strip, left side) are the Old Rhodes Key and Christmas Point, both of which are above water. The Caesar Creek bank is indicated by a red color, denoting depths of 2-4 ft. The Caesar Creek channel itself is shown in a bluish green color, denoting depths of 4-6 ft; this indication of extreme shallowness is attributed to the very turbid condition of the water in the Creek. The area around the Creek banks is correctly identified as being 4- to 6-ft deep. The deeper water off the eastern edge of the reef is clearly indicated as greater than 32-ft deep.

Off the end of the Creek, the water is shown in the lighter green color, which indicates depths of 6-8 ft. Toward the southeastern edge of the map, the dark blue color assigned to depths of 32 ft and above is predominant. The deeper water off the eastern edge of the reef is clearly indicated as greater than 32-ft deep.

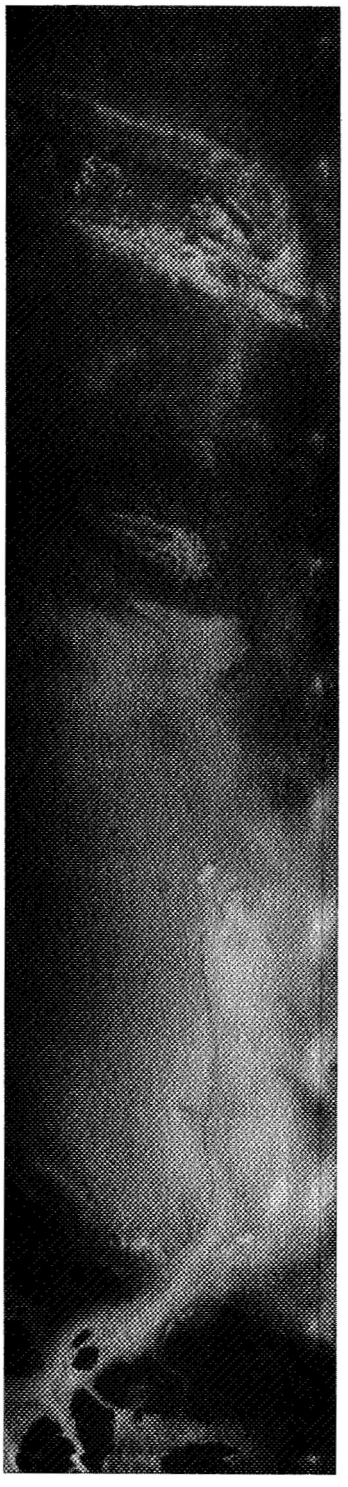

FIGURE 24. PRINTOUT OF 0.50-0.52 μm DATA FOR FLIGHT LINE FROM CAESAR CREEK TO AJAX REEF

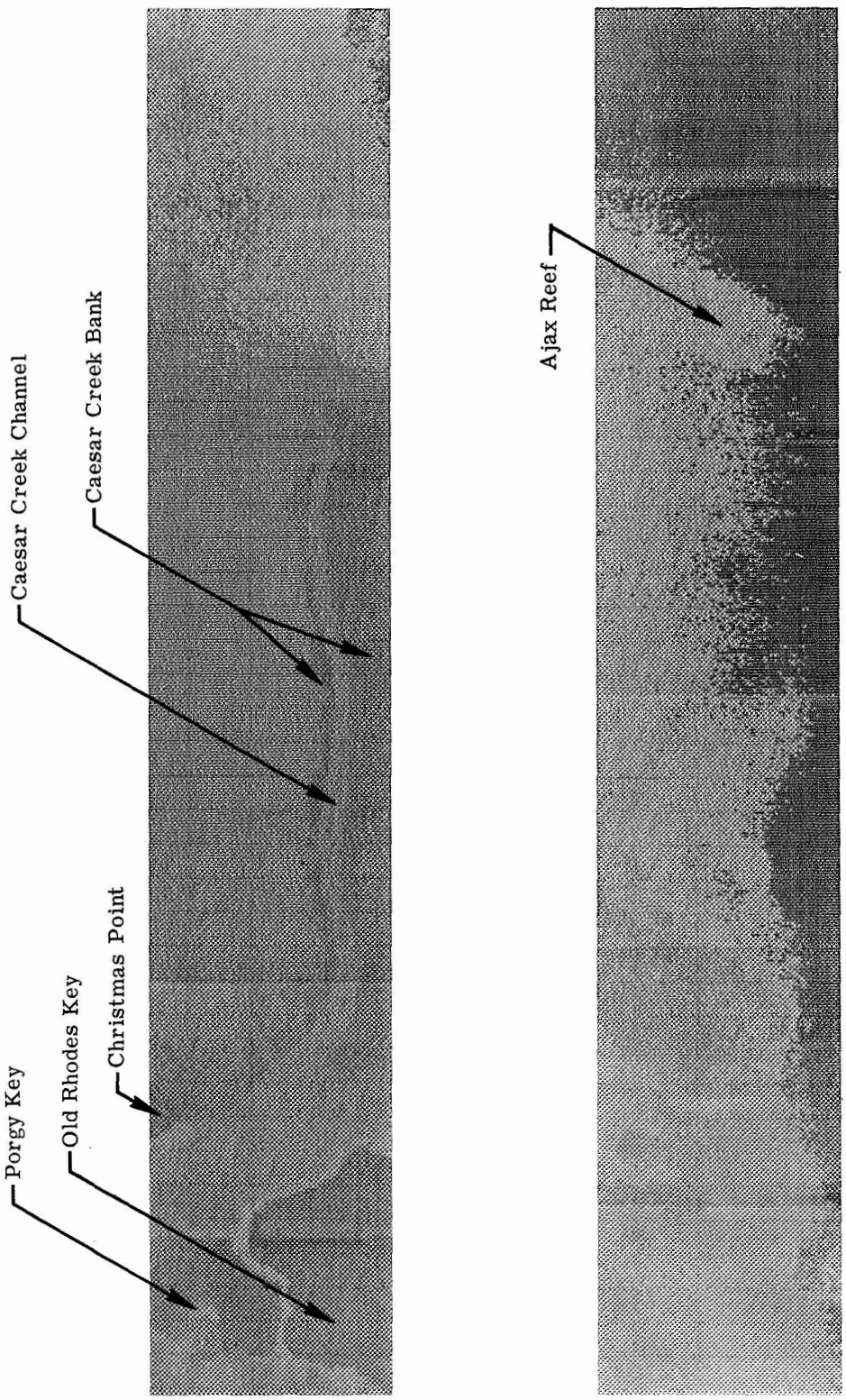

FIGURE 25. CONTINUOUS-STRIP, COMPUTER-GENERATED DEPTH CHART OF CAESAR CREEK/AJAX REEF AREA (COLOR CODED)

The map shown in Fig. 25 was generated from 6500-ft altitude data. The channel pairs (cf. Section 3.1) we used were as follows: 2-4; 2-5; 2-7; 4-5; 4-7; 5-7. Four of these (2-7, 4-5, 4-7 and 5-7) were chosen on the basis of uniformity of $\alpha_j - \alpha_i$; another (2-5) was chosen because of its uniformity in ρ_j/ρ_i; the sixth pair (2-4) was put in to test for sensitivity to water and/or bottom type variations.

Technical difficulties precluded finishing all the tests which had been planned. A run in which only the 3 best channel pairs were used had been planned, but was not finished in time for inclusion in this report. A comparison of 1967 data with 1970 data had been planned, as well as altitude comparisons. All of these were delayed because of technical difficulties which we believe now to be remedied. Pressures to modify both hardware and software associated with our CDC-1604 computer, plus reliability problems with the computer itself (encountered during the warm and humid July-August weather), slowed down production of tangible results. A brief description of the software modifications made during this contract is given below.

Hardware And Software Modifications. The spectral components of the radiant power passing through the shallow water are, in general, much less attenuated than the deep-water spectral components (scattering) which must be subtracted prior to final processing. The dynamic range of the signal creates problems during data collection, since the maximum range of the recorded signal is held within ±1 V, leading to a 2-V peak-to-peak maximum signal amplitude. If 80% of the signal is background (as it usually is in water-depth studies) then the remaining 1/2-V or so leads to a dynamic range of 25 quantum levels in A/D conversion. The signal is, in general, very noisy and not conducive to accurate measurements.

Until recently, it was not possible to introduce gain to the signal prior to A/D conversion. During the contract period, equipment modifications were made which allowed us to introduce a gain of 2 or 4, prior to digitization, thus improving the dynamic range of our depth data to 50 to 100 quantum levels. Previously, it was not uncommon for a small signal change to cause a 1- to 5-ft error in the depth measurement after quantization. Now, these errors can easily be held to 1 ft or less.

The computer program used to determine the angular correction for atmospheric and water-surface effects was modified to enable a fourth-order least-squares fit to the deep-water data. (Previously only a second-order fit was available). This modification enabled us to simulate a sec θ correction for angles up to ±50° instead of the ±20° provided by the earlier programs.

New, faster programs for generating the depth outputs were written, which made it possible to calculate depths for up to 36 channel-pair combinations with relative ease. The restriction of calculations to the 3 best pairs would make the processing of vast quantities of data in reasonably short time periods feasible, where it once would have been prohibitive.

Finally, the programs involved in the water-depth measurements have been integrated into a "systems" approach, which makes processing both more efficient and more reliable.

4
CONCLUSIONS

The two remote sensing methods for water-depth determination described herein have been proven to be feasible within certain operational constraints. The wave-refraction method depends on the existence of a set of wave swells the wave length of which is long enough to be affected by the presence of a shallow feature. On the other hand, since the technique does not depend on light transmission in the water and bottom reflection, it offers a depth-measurement capability in areas too turbid for the multispectral ratio technique or the laser pulse-ranging method. As the altitude increases, even to satellite altitudes, the wave-refraction method still retains potential (within limitations of resolution). In some cases, the analysis of the Fourier transform domain becomes simpler because, with the small scale photography, the imaging of wave lengths as a higher frequency in the transfer domain is possible. It is expected that the technique will be useful in locating the existence of shallow features, such as sandbar shoals, reefs, or sea mounts, and in some cases, will provide an estimate of depth.

As a complementary method to provide a depth measurement at all image points at which a bottom reflection can be measured, the multispectral ratio technique is being developed. Depth charts can be generated by this technique, as shown in Fig. 25. The averages assumed for attenuation coefficients and reflectance of the bottom materials can be made more accurate by the use of a priori knowledge of sampled depths within the scene.

The wave-refraction method is one way that an independent depth in the scene can be measured. The use of a laser pulse-ranging system is another. The equation for depth (using the multispectral ratio technique) is then solved for the unknown constants. Since the depth is known at several points, the complete map can be made with greater accuracy.

The development of this multisensor system offers the maximum potential for realization of an airborne/spaceborne system of remote measurement of shallow water features.

Appendix I
REVIEW OF IMAGERY FROM MISSION No. 98

I. Summary of Mission Imagery

Willow Run Laboratories received five reels of sensor imagery which covered the flight lines over Puerto Rico (site 92), Barbados (site 192), and an additional run from St. John to St. Croix. In general, the imagery was of very good quality; specific exceptions will be noted later. The flight coverage was best in four areas: (1) the south shore of Puerto Rico, from Ponce to Punta Tuna; (2) the island chain running from Cabo San Juan to Grampus Shoals; (3) the sea (offshore) area immediately south of St. Croix; and, (4) the flight lines around Barbados.

The flight imagery along the western and northern coasts of Puerto Rico, Mona Island, and that between St. John and St. Croix was generally not as good. The summary below discusses specific imagery in more detail and outlines its possible value toward the achievement of mission objectives. Frames from this mission were used in experiments for depth measurement (Section 2).

A. RC-8 Color Ektachrome 2448

Good, clear imagery was obtained with approximately 40-ft water-depth penetration in some areas, with generally excellent juxtaposition of sunspot-glitter pattern on imagery frames. The apparently calm sea state along the northern shore of Puerto Rico may indicate a marginal use of the data for Fourier analysis of wave action. The southern shoreline flight at 5000 ft shows excellent promise for Fourier analysis, as does the run from Cabo San Juan to Grampus Shoals.

There is an excellent coverage of the entire shoreline of Barbados and very good water-depth penetration, up to at least 50 ft in some cases. The Bridgetown harbor bottom is well defined up to 40 ft (e. g., Pelican and Long shoals are clearly visible). The sunspot position is good on all frames.

B. RC-8 Color IR SO117

The obvious advantage of Color IR is that it allows discrimination between the land/water boundary but shows little or no water-depth penetration. The sunspot contrast with surrounding water features is very good and the wave state within the sunspot is usually well defined.

The sunspot position along the west coast and the south coast, from Cabo Rojo to Punta Petrona, is not as well placed as seen in other film rolls, but the flight lines from Punta Petrona to Punta Tuna and from Cabo San Juan to Grampus Shoals are very good in this respect. The flight line to Mona Island appears to be of marginal value for wave analysis, as the sunspot is only partially recorded in each frame.*

*The film containing the Mona Island IR imagery was found damaged upon its receipt at the Willow Run Laboratories. (Frames 6309 -11, -12, -13, -15, -16, -17, -19, -20)

C. D-500 Two Layer Emulsion

This imagery, like the Color Ektachrome, generally displayed good sunspot position on each frame, a sharp contrast of wave features within the sunspot, and water-depth penetration. The bottom topography south and east of Cabo Rojo is observable to 50 ft, although the sunspot, in this instance, is not centered on the frame. The imagery between St. John and St. Croix is very good, and there is excellent depth penetration south of St. Croix (40 ft +). The flight lines around Barbados are generally fine and should compliment the Ektachrome imagery in our analysis of shoal areas surrounding this island.

D-1. KA62 A, Filter 25A

This film-filter combination gives a good definition of shore (land) features and a sunspot that contrasts well with surrounding water features. There is, however, negligible water-depth penetration.

D-2. KA62 B, Filter 47B

We have very good water-depth penetration with this combination (50 ft +), but at the expense of poor wave contrast within the sunspot-glitter pattern.

D-3. KA62 C, Filter 58

Good water-depth penetration (40 ft +) is provided, but the sunspot contrasts only moderately with surrounding water features. In some instances, the sunspot position is not effectively placed.

D-4. KA62 D, Filter 89B

Very high contrast between the sunspot and surrounding water features is evident. There is excellent discrimination between the water/land boundary and good detail of land features. Water-depth penetration is negligible.

E. RS-14 (8-14 μm)

No indications of thermal gradients associated with shallow waters or with currents are seen. Apparently the contrast settings were not set to observe small temperature differences.

F. DPD-2 SLAR

No wave action or depth penetration is observable. Again, it is possible that the radar-signal dynamic range was set for land features and not for water wave-surface detail.

Appendix II
EMPIRICAL DETERMINATION OF ATTENUATION COEFFICIENTS AND BOTTOM REFLECTANCES

Where fairly accurate water-depth measurements are available, either from soundings or in-flight laser bathymetry measurements, it is possible to determine water and bottom data directly from the scanner data.

The depth equation (cf., Eq. 9) can be written as follows:

$$\Delta V_{ij} = (V_{ij})_{ss} \rho_{ij} e^{-f(\theta, \phi)\alpha_{ij} Z} \tag{11}$$

where

$$\Delta V_{ij} = \frac{\Delta V_i}{\Delta V_j}$$

$$(V_{ij})_{ss} = \frac{[V_i/\rho(\lambda_i)]_{ss}}{[V_j/\rho(\lambda_j)]_{ss}}$$

$$\rho_{ij} = \frac{\rho(\lambda_i)}{\rho(\lambda_j)}$$

$$f(\theta, \phi) = \sec \theta + \sec \phi$$

$$\alpha_{ij} = \alpha_i - \alpha_j$$

By taking the derivative of (11) we obtain

$$\frac{\partial(V_{ij})}{\partial Z} = -f(\theta, \phi) V_{ij} \alpha_{ij} \tag{12}$$

If we solve the above expressions for α_{ij} and ρ_{ij}, then we have

$$\alpha_i - \alpha_j = \frac{\left[\left(\frac{\Delta V_i}{\Delta V_j}\right)_{Z_1} - \left(\frac{\Delta V_i}{\Delta V_j}\right)_{Z_2}\right]}{1/2(\sec \theta + \sec \phi)(Z_2 - Z_1)\left[\left(\frac{\Delta V_i}{\Delta V_j}\right)_{Z_1} + \left(\frac{\Delta V_i}{\Delta V_j}\right)_{Z_2}\right]} \tag{13}$$

and

$$\rho_i/\rho_j = \frac{\left(\frac{\Delta V_i}{\Delta V_j}\right) e^{(\sec \theta + \sec \phi)(\alpha_i - \alpha_j)Z}}{\left\{\frac{[V_i/\rho(\lambda_i)]_{ss}}{[V_j/\rho(\lambda_j)]_{ss}}\right\}} \tag{14}$$

These expressions are, of course, approximate, but, nevertheless, are very reliable if the difference of Z_1 and Z_2 is small compared to the average of Z_1 and Z_2.

REFERENCES

1. F. C. Polcyn and R. A. Rollin, Remote Sensing Techniques for the Location and Measurement of Shallow-Water Features, Report No. 8973-10-P, Willow Run Laboratories of the Institute of Science and Technology, The University of Michigan, Ann Arbor, January 1969.
2. F. C. Polcyn, W. Brown, and I. Sattinger, The Measurement of Water Depth by Remote Sensing Techniques (Final Report), Report No. 8973-26-F, Willow Run Laboratories of the Institute of Science and Technology, The University of Michigan, Ann Arbor, November 1970.
3. Breakers and Surf, Principles in Forecasting, U. S. Naval Oceanographic Office, H. O. Pub., No. 234, 1958.
4. J. W. Johnson, et al., Graphic Construction of Wave Refraction Diagrams, U. S. Naval Oceanographic Office, H. O. Pub., No. 605, January 1948.
5. N. F. Barber, "A Diffraction Analysis of a Photograph of the Sea," Nature, Vol. 164, 1949, p. 485.
6. C. Cox and W. H. Munk, "Statistics of the Sea Surface Derived from Sun Glitter," J. Marine Res., Vol. 13, No. 2, pp. 198-227, 1954, p. 213.
7. V. Noble, "Ocean Swell Measurements From Satellite Photographs," R. S. E., Vol. 1, No. 3, Summer 1970, pp. 151-154.
8. G. C. Lendaus and G. L. Stanley, "Diffraction-Pattern Sampling for Automatic Pattern Recognition," Proceedings of IEEE, Vol. 58, No. 2, February 1970, pp. 198-216.

BIBLIOGRAPHY

Barber, N. F., "A Diffraction Analysis of a Photograph of the Sea", Nature, Vol. 164, 1949, p. 485.

Barber, N. F., "Experimental Correlograms and Fourier Transforms," International Tracks in Computer Science and Technology and Their Application, Vol. 5, Pergamon Press, New York, N. Y., 1961.

Breakers and Surf, Principles in Forecasting, U. S. Naval Oceanographic Office, H. O. Pub., No. 234, 1958.

Cox, C. and W. H. Munk, "Statistics of the Sea Surface Derived from Sun Glitter," J. Marine Res., Vol. 13, No. 2, 1954, pp. 198-227.

Goodman, Joseph W., Introduction to Fourier Optics (No. 4), McGraw Hill, New York, N. Y., 1968.

Johnson, J. W., et al., Graphical Construction of Wave Refraction Diagrams, U. S. Naval Oceanographic Office, H. O., Pub. No. 605, January 1948.

Lendaus, George G. and Gordon L. Stanley, "Diffraction-Pattern Sampling for Automatic Pattern Recognition," Proceedings of the IEEE, Vol. 58, No. 2, February 1970, pp. 198-216.

Manual of Photographic Interpretation, ed. by R. N. Colwell, ASP, Wash., D. C., 1960.

Polcyn, F. C., W. Brown, and I. Sattinger, The Measurement of Water Depth by Remote Sensing Techniques (Final Report), Report No. 8973-26-F, Willow Run Laboratories of the Institute of Science Technology, The University of Michigan, Ann Arbor, November 1970.

Polcyn, F. C. and R. A. Rollin, Remote Sensing Techniques for the Location and Measurement of Shallow-Water Features, Report No. 8973-10-P, Willow Run Laboratories of the Institute of Science and Technology, The University of Michigan, Ann Arbor, January 1969.

Stilwell, D., Jr., "Directional Energy Spectra of the Sea from Photographs," J. Geophys. Res., Vol. 74, No. 8, April 15, 1969, pp. 1974-1986.

Stoker, J. J., Water Waves — The Mathematical Theory with Applications, Interscience Publications, Inc., New York, N. Y., 1957.

DISTRIBUTION LIST

NASA Manned Spacecraft Center
Earth Observations Division
Houston, Texas 77058

ATTN: Larry York/TF, Contract: NAS 9-9784 — 4
A. E. Potter/TF3, Contract: NAS 9-9784 — 1
W. E. Hensley/TD, Contract: NAS 9-9784 — 1

NASA Manned Spacecraft Center
Space Sciences Procurement Branch
Houston, Texas 77058

ATTN: R. F. LaMere BB321 (S55), Contract: NAS 9-9784

Dr. Archibald Park
Chief, Earth Research Survey Program
NASA Headquarters
Washington, D. C. — 1

Dr. Robert Miller
U. S. Department of Agriculture
Washington, D. C. — 1

Dr. Craig Wiegand
U. S. Department of Agriculture
Agricultural Research Service
Soil and Water Conservation Research Division
P. O. Box 267
Weslaco, Texas 78596

Dr. Arch C. Gerlach
U. S. Department of Interior
Geological Survey
Washington, D. C. 20242

Dr. Willaim Hemphill
USGS
Branch of Theoretical Geophysics
2221 Jefferson Davis Highway
Arlington, Virginia 22202

Mr. C. J. Robinove
Code 4032 0001
Water Resources Division
U. S. Geological Survey
Washington, D. C. 20242

Dr. Raymond W. Fary
U. S. Department of Interior
Geological Survey
801 19th Street, N. W., Room 1032
Washington, D. C. 20242

Mr. Charles Withington
U. S. Department of Interior
Geological Survey
801 19th Street, N. W.
Washington, D. C. 20242

Mr. M. Deutsch
U. S. Department of Interior
Geological Survey
801 19th Street, N. W.
Washington, D. C. 20242

Dr. Jules D. Friedman
U. S. Geological Survey
801 19th Street, N. W. Room 1030
Washington, D. C. 20242

Dr. A. Campbell/Dr. Harry W. Smedes
U. S. Department of Interior
Geological Survey
Federal Center
Denver, Colorado 80225

Mr. Aaron L. Higer/Mr. Milton Kolipinski
U. S. Department of Interior
Geological Survey
Water Resources Division
Room 730, 51 S. W., First Avenue
Miami, Florida 33130

Dr. Robert Colwell
University of California
School of Forestry
Berkeley, California 94720

Dr. Charles E. Poulton
Range Management
School of Agriculture
Oregon State University
Corvallis, Oregon 97331

Mr. Robert MacDonald
Laboratories of Agricultural Remote Sensing
McClure Research Park
1220 Potter Drive
West Lafayette, Indiana 47906

Mr. R. C. Heller/Dr. P. Weber
Pacific Southwest Forest and Range Experiment Station
U. S. Forest Service
P. O. Box 245
Berkeley, California 94701

John D. Overton TF4/EOD
NASA Manned Spacecraft Center
Houston, Texas 77001

Mr. Victor I. Myers
Director, Remote Sensing Institute
South Dakota State University
Agriculture Engineering Building
Brookings, S. D. 57006

Mr. Marvin Holter
Chief, Earth Observations Division
NASA Manned Spacecraft Center
Houston, Texas 77058

Harvey K. Nelson
U. S. Department of Interior
Fish and Wildlife Service
Bureau of Sport Fisheries and Wildlife
Northern Prairie Wildlife Research Center
Jamestown, N. D. 58401

Richard Driscoll
Forest Service
U. S. Department of Agriculture
240 West Prospect Street
Fort Collins, Colorado 80521

A. E. Coker
U. S. Department of Interior, Geological Survey
Water Resources Division
500 Zack Street
Tampa, Florida 33602

Kenneth Watson
U. S. Geological Survey
Branch of Regional Geophysics
Denver Federal Center, Building 25
Denver, Colorado 80225

Mr. Edward O. Zeithler TF/12
Chief, Earth Resources
Research Data Facility
NASA Manned Spacecraft Center
Houston, Texas 77058 — 12

Defense Documentation Center
Cameron Station
Alexandria, Virginia 22314 — 12

NASA Scientific and Technical Information Facility
Box 33
College Park, Maryland 20740 — 2

Naval Oceanographic Office
Code 17
Washington, D. C. 20390 — 2

Receiving Officer
Naval Oceanographic Office
Washington, D. C. 20390

ATTN: Code 707, J. W. Sherman — 100